










## RESEARCH ARTICLE

10.1029/2023EA002878

### Special Section:

Twenty Years of Observations from the Atmospheric Infrared Sounder

# Comparison of the AIRS, IASI, and CrIS Infrared Sounders Using Simultaneous Nadir Overpasses: Novel Methods Applied to Data From 1 October 2019 to 1 October 2020

M. Loveless<sup>1</sup> , R. Knuteson<sup>1</sup> , H. Revercomb<sup>1</sup>, L. Borg<sup>1</sup> , D. DeSlover<sup>1</sup> , G. Martin<sup>1</sup>, J. Taylor<sup>1</sup> , F. Iturbide-Sanchez<sup>2</sup> , and D. Tobin<sup>1</sup> 

<sup>1</sup>Space Science and Engineering Center, University of Wisconsin—Madison, Madison, WI, USA, <sup>2</sup>NOAA/NESDIS/Center for Satellite Applications and Research (STAR), College Park, MD, USA

### Key Points:

- Simultaneous nadir overpass comparisons include time difference symmetrization, spatial sampling uncertainty, and Cross-track Infrared Sounder (CrIS) radiometric uncertainty
- Differences between Suomi National Polar-Orbiting Partnership (SNPP) CrIS and NOAA-20 CrIS are generally less than 0.1 K and within combined radiometric measurement uncertainties
- Differences between Atmospheric Infrared Sounder (AIRS) and CrIS or AIRS and Infrared Atmospheric Sounding Interferometer (IASI) generally less than 0.4 K, differences between CrIS and IASI generally less than 0.25 K

### Supporting Information:

Supporting Information may be found in the online version of this article.

### Correspondence to:

M. Loveless and D. Tobin,  
[michelle.loveless@ssec.wisc.edu](mailto:michelle.loveless@ssec.wisc.edu);  
[dave.tobin@ssec.wisc.edu](mailto:dave.tobin@ssec.wisc.edu)

### Citation:

Loveless, M., Knuteson, R., Revercomb, H., Borg, L., DeSlover, D., Martin, G., et al. (2023). Comparison of the AIRS, IASI, and CrIS infrared sounders using simultaneous nadir overpasses: Novel methods applied to data from 1 October 2019 to 1 October 2020. *Earth and Space Science*, 10, e2023EA002878. <https://doi.org/10.1029/2023EA002878>

© 2023 The Authors. Earth and Space Science published by Wiley Periodicals LLC on behalf of American Geophysical Union.

This is an open access article under the terms of the [Creative Commons Attribution-NonCommercial-NoDerivs License](https://creativecommons.org/licenses/by/4.0/), which permits use and distribution in any medium, provided the original work is properly cited, the use is non-commercial and no modifications or adaptations are made.

**Abstract** High spectral resolution infrared sounders are an integral component of the global observing system and are used in a broad range of applications. This is enabled by their high accuracies which are ensured by rigorous calibration/validation activities. One of these activities is the post-launch intercomparison with other high spectral resolution infrared sounders using simultaneous nadir overpasses (SNOs). This paper introduces a novel application of the previously developed SNO methodology by including time difference histogram symmetrization and a spatial sampling uncertainty. Where possible, radiometric measurement uncertainties are included and propagated through the statistics. Comparisons of Atmospheric Infrared Sounder (AIRS), METOP-A/B/C Infrared Atmospheric Sounding Interferometer (IASI), and Cross-track Infrared Sounder (CrIS) from 1 October 2019, to 1 October 2020, are analyzed. Results show AIRS and IASI differences as well as CrIS and AIRS differences are generally less than 0.4 K across the spectrum, and CrIS and IASI differences are generally less than 0.25 K. Comparison of the Suomi National Polar-Orbiting Partnership and NOAA-20 CrIS instruments via IASI and AIRS shows differences are generally less than 0.1 K across all bands and that the two CrIS instruments statistically agree within their radiometric uncertainties except for the narrow 2,370 cm<sup>-1</sup> region where artifacts due to brightness temperature conversion are prone to occur.

**Plain Language Summary** One of the primary sources of information used to monitor Earth's weather patterns are satellite based meteorological instruments that measure radiation in the infrared region with high spectral resolution. Agencies worldwide use data from these types of instruments to provide input into weather prediction models. The long term data sets are also very valuable for multi-decadal climate studies. To ensure the value of these data, the instruments need to be properly calibrated using external references. This paper details and expands upon the previously established methodology of one commonly used calibration technique—called SNOs. This method compares nadir-viewing data from different instruments measuring radiation coming from the same mass of atmosphere in time and space. Introduced in this paper are two additions to the methodology: (a) a symmetrization of the time differences between when the instruments measure the specific air mass, and (b) an uncertainty estimate on the comparison based on the spatial coincidence of the measurements. Results from this methodology demonstration show how well the current suite of satellite-based instrumentation measuring infrared radiation at high spectral resolution agree with each other.

## 1. Introduction

High spectral resolution infrared sounders are an integral component of the global Earth observing system. Since the launch of the first of these instruments into space, the Atmospheric Infrared Sounder (AIRS) in 2002, several others have been developed and launched into space with the primary goal of supporting medium-range weather forecasting. Two of these instruments include the Infrared Atmospheric Sounding Interferometer (IASI) series and the Cross-track Infrared Sounder (CrIS) series. The AIRS, IASI, and CrIS high spectral resolution infrared sounders (hereafter simply referred to as “IR sounders”) comprise all that are being used by the U.S. operational system for medium-range weather forecasting. These instruments, however, are also highly valuable in other types of applications, including nowcasting (e.g., Berndt et al., 2020; Bloch et al., 2019; Maier & Knuteson, 2022; W. L. Smith et al., 2020), climate trending (e.g., Brindley et al., 2015), climate model assessment (e.g., Della Fera

Received 8 FEB 2023  
Accepted 26 JUN 2023

**Author Contributions:**

**Conceptualization:** H. Revercomb, D. Tobin  
**Data curation:** D. DeSlover  
**Formal analysis:** M. Loveless, R. Knuteson  
**Funding acquisition:** F. Iturbide-Sanchez, D. Tobin  
**Methodology:** M. Loveless, R. Knuteson, H. Revercomb, J. Taylor, D. Tobin  
**Project Administration:** F. Iturbide-Sanchez, D. Tobin  
**Visualization:** M. Loveless, R. Knuteson  
**Writing – original draft:** M. Loveless, R. Knuteson  
**Writing – review & editing:** M. Loveless, R. Knuteson, H. Revercomb, L. Borg, D. DeSlover, G. Martin, J. Taylor, F. Iturbide-Sanchez, D. Tobin

et al., 2022) satellite intercalibration (Goldberg et al., 2011; Gyanesh et al., 2013), and trace gas retrievals (e.g., Payne et al., 2022; N. Smith & Barnet, 2020; Worden et al., 2022).

The use of these instruments in such a broad range of applications is enabled by their accuracies and the rich amount of information contained in their measurements. Accuracy of these instruments is ensured by rigorous calibration and validation of the measurements both pre- and post-launch. For each instrument radiometric (e.g., Aumann et al., 2006; Pagano et al., 2003; Tobin et al., 2013a), spectral (e.g., Chen et al., 2016; Strow et al., 2003, 2013), and geolocation (e.g., Wang et al., 2013; Wang et al., 2017) calibrations are performed. The ability to assign uncertainties (which are tied back to absolute standards) to these types of calibrations add additional value to the measurements. While International System of Units (SI) traceability to a National Institute of Standards and Technology (NIST) standard is the most accurate and straightforward way to assess the accuracy of an instrument, another way is via intercalibration. Intercalibration is achieved by calibrating an instrument such that its measurements match those of a reference instrument, which has a higher accuracy and well-defined uncertainties. While a high spectral resolution infrared reference sensor named the Absolute Radiance Interferometer (Taylor et al., 2020) was developed under NASA's Earth Science Technology Office as part of the Climate Absolute Radiance and Refractivity Observatory (CLARREO) mission, it was not funded to be launched into space. Having such an instrument in orbit would provide a way to tie the current system of IR sounders together, creating a climate quality product with well-defined absolute uncertainties (Tobin et al., 2016).

Despite this, intercomparison between existing IR sounders is still a key aspect of post-launch calibration activities. Comparisons between these instruments can be obtained in different ways, but the one that is the most direct is via simultaneous nadir overpasses (SNOs). SNOs were first used in the intercalibration of lower spectral resolution radiometers like HIRS (e.g., Cao et al., 2004; Cao, Ciren, et al., 2005; Cao, Goldberg, et al., 2005; Wang et al., 2007), but this method has been adopted for use in comparing measurements from all types of satellite-based instruments. SNOs were quickly adopted for use in the comparison of high spectral resolution IR sounders to each other when AIRS and IASI were both first in orbit together (e.g., Blumstein et al., 2007; Iacovazzi & Cao, 2008; Tobin et al., 2010; Wang et al., 2011), and have persisted to be an important calibration/validation activity for subsequent IR sounders like CrIS (Tobin et al., 2013b; Wang et al., 2015).

This paper details a recent comparison of the AIRS, three IASI instruments, and two CrIS instruments being flown in space from 1 October 2019 to 1 October 2020, using SNOs. This time period was selected as the only continuous 12-month period where all six sensors were operating with optimal calibration performance. This paper introduces an updated comparison methodology, which includes a spatial sampling uncertainty analysis adopted and modified from previous publications (Taylor et al., 2020; Tobin et al., 2016). Where possible, RU is also considered and properly propagated through the statistics. Section 2 describes the radiance products analyzed, Section 3 outlines the comparison methodologies, Section 4 details the novel application of the SNO sampling uncertainty theory, Section 5 contains results of the high latitude SNO comparisons, Section 6 contains results of the CrIS and AIRS orbit phase dependence, and Section 7 concludes the paper.

## 2. Radiance Products and Uncertainties

### 2.1. NASA CrIS L1B Version 3

CrIS is a Fourier transform spectrometer being flown on the operational Joint Polar Satellite System satellite series, including the Suomi National Polar-Orbiting Partnership (SNPP) satellite, the NOAA-20 satellite and three subsequent satellites. It measures infrared radiances across three spectral regions spanning 650 to 2,550  $\text{cm}^{-1}$ . It has a scan range of  $\pm 50^\circ$  and its horizontal resolution at nadir is approximately 14 km. SNPP and NOAA-20 CrIS radiance products are currently produced by both NOAA and NASA. Since the launch of the first CrIS in 2011, NOAA has provided operational, real-time CrIS radiance products to numerical weather centers around the globe with the goals of speed, reliability, and accuracy in mind. The NOAA radiance products are produced using the Interface Data Processing Segment software system and are available to the public through the NOAA Comprehensive Large Array-Data Stewardship System archive.

NASA maintains a climate-quality CrIS radiance product which highlights software transparency and can be reprocessed often with calibration updates. Additionally, starting with Version 3, the NASA CrIS radiance product has accompanying publicly available software which can be used to create the CrIS RU for every field of view (FOV) and spectral channel using a methodology that adheres to the accepted metrology guidelines for

assessing measurement uncertainty ([https://docserver.gesdisc.eosdis.nasa.gov/public/project/Sounder/NASA\\_CrIS\\_L1B\\_Radiometric\\_Uncertainty\\_v3.pdf](https://docserver.gesdisc.eosdis.nasa.gov/public/project/Sounder/NASA_CrIS_L1B_Radiometric_Uncertainty_v3.pdf)). As described by Tobin et al. (2013a), the radiometric uncertainty (RU) characterizes the accuracy of the observed radiance spectra. RU represents an upper limit of the bias with respect to the true radiance and does not include effects such as detector noise which vary randomly from one spectrum to another.

For the studies shown in this paper, the NASA CrIS L1B Version 3 was selected due to its use of a single algorithm version for both SNPP and NOAA-20 CrIS data records and the availability of RU parameters for every footprint (UW-Madison, 2022). The NASA L1B radiance product can be found at the Goddard Earth Sciences Data and Information Services Center (GESDISC), and the product software was written by the CrIS L1B Science and Software Team, located at the University of Wisconsin-Madison Space Science and Engineering Center and the University of Maryland Baltimore County Atmospheric Spectroscopy Laboratory. Full Spectral Resolution (FSR) CrIS data from SNPP (Revercomb & Strow, 2020b) and NOAA-20 (Revercomb & Strow, 2020a) satellites are used. The FSR product reports radiances on a fixed wavenumber grid of 650–2,550  $\text{cm}^{-1}$  and has a spatial resolution of 0.625  $\text{cm}^{-1}$ .

## 2.2. NASA AIRS L1C V6.7

AIRS is a hyperspectral infrared grating spectrometer onboard NASA's Aqua satellite which was launched in 2002. AIRS has a spectral coverage of 649–2,702  $\text{cm}^{-1}$  and a nominal resolving power of 1200 (Aumann et al., 2020). AIRS has a cross track scan of 49.5° and a spatial resolution at nadir of about 13.5 km.

The NASA AIRS Level 1C (L1C) radiance product, labeled "AIRICRAD," is used in this study and is available online through the Goddard Distributed Active Archive Center. The AIRS L1C Version 6 products are based on the AIRS L1B Version 5 product which contains measured radiances for 2,378 channels which have center wavenumbers that drift over time (Aumann et al., 2020). The AIRS L1C Version 6 products contain additional, synthesized radiances for channels within spectral gaps, with dead detectors, or with excessive noise for a total of 2,645 channels. The AIRS L1C Version 6.7 product (Strow, 2019), which is used in this study, builds upon the Version 6 product, and includes slightly adjusted radiances from the AIRS L1B Version 5 product to account for temporal changes in the channel center wavenumber. Corresponding spectral response functions for the AIRS L1C product are used in the study (Strow, 2020).

AIRS uncertainty estimates from Pagano et al. (2020) are used in this paper for interpretation of the sounder radiance differences. It is important to note that the uncertainty estimates are for the Version 5 product but should have overall similar characteristics and magnitudes to the Version 6 products. As noted by Pagano et al. (2020) "For temperatures greater than 260 K, the measurement uncertainty is better than 250 mK  $1\sigma$  for most channels." Much of the analysis done in this paper, due to the nature of the spatial collocation used, however, uses radiance measurements for scene temperatures between 210 and 260 K. At these colder temperatures, AIRS uncertainties depend much more on the detector module, but in general are less than 1 K  $1\sigma$  for most channels (with exceptions primarily including SW channels). Readers are referred to Figure 8 of Pagano et al. (2020) for more quantitative values.

## 2.3. EUMETSAT IASI L1C

IASI is a Fourier transform spectrometer which has been flying on the Metop series of satellites since 2006 (Hilton et al., 2012). The IASI radiance product has 8,461 spectral channels within the infrared region covering 645–2,760  $\text{cm}^{-1}$  and a spectral sampling of 0.25  $\text{cm}^{-1}$ . IASI has a spatial resolution of ~12 km at nadir and a scan range of ~48°.

Relevant to this study, the Metop-B and Metop-A IASIs had their nonlinearity corrections updated on 2 August 2017 and 30 September 2019 respectively. These updates had detectable impacts on the IASI longwave radiances when IASI is compared to both AIRS and CrIS via SNOs. Thus, to use data from only the most current and best-knowledge calibration time periods, only IASI data collected after the IASI-A and IASI-B nonlinearity update is used.

The IASI Level 1C (L1C) radiance product is used in this study and contains geolocated, calibrated, resampled and apodized radiance spectra (EUMETSAT, 2009). IASI radiances from Metop-A, Metop-B, and Metop-C

platforms are obtained through EUMETSAT from the IASI GDS L1C files (<https://navigator.eumetsat.int/product/EO:EUM:DAT:METOP:IASI:L1C-ALL>). The general quality flag variable, “GQisFlagQual” is used to quality control the data. While this study makes use of the gaussian apodized radiance product, the apodization is removed before degrading IASI's spectral resolution to match that of AIRS and CrIS as described in a following section. While there is currently no publicly available RU product available for IASI, the Center National D'Etudes Spatiales (CNES) have been developing an uncertainty analysis of the IASI calibration (Kilymis et al., 2023). This should be included in future analysis once it is available.

### 3. Methods

#### 3.1. Big Circle SNO Method

The rationale for the methodology used in the comparison of AIRS and CrIS is described in Tobin et al. (2016). By including multiple sounding footprints of each sensor in a “big circle” (or ellipse if off-axis) the spatial sampling uncertainty in the mean is reduced significantly compared to that of a comparison between single sounder footprints. For each “big circle” SNO the distribution of radiances is approximately Gaussian, primarily due to the pseudo random nature of cloud fields in such a limited domain. Figure 3 of Tobin et al. (2016) illustrates the concept of a big circle very nicely. The approach described in Tobin et al. (2016) and Taylor et al. (2020) has been extended to the CrIS/IASI and AIRS/IASI SNOs. For each big circle SNO, the mean and standard deviation of the radiance spectra are recorded for both sensors.

Due to the orbital characteristics of the AIRS, IASI, and CrIS platforms, namely that CrIS and AIRS share an orbit local time (1330 UTC), but with different altitudes (833 and 705 km), while IASI has its own orbit local time (0930 UTC), the geographic distribution of the CrIS/AIRS SNOs differs from that of the CrIS/IASI and AIRS/IASI SNOs. The AIRS/IASI and CrIS/IASI SNOs form latitudinal rings centered around  $\sim\pm 75^\circ$  North and are spread evenly across all longitudes. The CrIS/AIRS SNOs are also mainly at high latitudes but because the sensors are at different orbital altitudes with the same equatorial crossing time CrIS/AIRS SNOs exist at nearly all latitudes.

For this study, CrIS/IASI and AIRS/IASI SNOs are found using UW-Madison SSEC's OrbNav tool (<https://sips.ssec.wisc.edu/orbnav/#/>; Nagle & Holz, 2009). To retain an ample number of samples but minimize temporal mismatch, a 60-min time difference restriction is applied to the AIRS-IASI and CrIS-IASI SNO overpass time differences. Data for each instrument, within a 100 km radius of the SNO latitude and longitude, is then collected. For each IASI and CrIS, the full  $2 \times 2$  and  $3 \times 3$  set of detectors respectively are maintained so that a similar number of samples is used from each detector. To facilitate this, the IASI FOV 4 and CrIS FOV 5 latitude and longitude points are used as the proxy location for all detectors in their arrays. For IASI, the choice of FOV number used for latitude/longitude data was arbitrary and should be looked at in future analyses (e.g., the mean of the detector array latitude/longitude could have been used for geolocation). Once the data for a single SNO are collected, any necessary spectral resolution conversions are applied, and lastly the average and standard deviation of the spectra over the big-circle are computed.

For the AIRS/CrIS SNOs, the orbits of the sensors are such that AIRS is at a lower altitude than CrIS (705 vs. 833 km) and the time match can be very small as one satellite overtakes the other approximately every three days. For this study the mean satellite zenith angle of the soundings within the big circle of each sensor must be within three degrees and the mean time difference less than 12 min.

#### 3.2. Spectral Resolution Reduction Methods

One necessary step in facilitating the sounder comparisons is converting the radiances from each instrument to a common spectral resolution. For the CrIS and IASI comparisons, IASI L1C radiances are converted to the CrIS FSR spectral resolution using a highly accurate and well-defined approach, enabled by the fact that both IASI and CrIS are interferometers, and IASI has a higher maximum optical path difference than CrIS. In this process, (a) the IASI L1C radiances are converted to interferograms via Fourier transform, (b) the IASI Gaussian apodization is removed from the interferograms, (c) the IASI interferograms are truncated to the CrIS FSR maximum optical path of 0.8 cm, and (d) the IASI interferograms are converted back to radiances via an inverse Fourier transform.

For the IASI and AIRS comparison, IASI L1C radiances are converted to AIRS resolution. Again, this process is well defined due to the fact that the maximum IASI optical path difference (2 cm) covers all delays contributing

to AIRS, except for the extreme tail of the longwave AIRS signal response functions (SRFs). The first steps in this process are the same as (a), (b), and (d) from above, where the Gaussian apodization is removed from the IASI L1C spectra in the interferogram domain. Lastly, the unapodized IASI radiances are oversampled and convolved with the AIRS L1C v6.7 SRFs (Strow, 2020). For the purposes of this study, the AIRS L1C radiances and IASI radiances convolved with the AIRS L1C SRFs are subset to only include channels from the AIRS L1B data set. This is done to avoid using the channels of the AIRS L1C product which are purely synthetic. Figure S1 in Supporting Information S1 shows the error associated with this spectral resolution conversion using a single monochromatic radiance calculation. It should be noted that this error does not account for the broad spectral deviations from zero that are seen in the IASI-minus-AIRS bias shown in subsequent sections of this paper. Motteler and Strow (2019) provide more detailed analysis of these spectral conversions.

For the comparison between CrIS and AIRS, CrIS FSR spectra are oversampled and convolved with the AIRS L1C v6.7 SRFs like in the case for AIRS and IASI. Again, both sets of spectra are then subset to the AIRS L1B channel set. While CrIS FSR has a somewhat higher effective spectral resolution than AIRS, AIRS has significant contributions from delays not measured by CrIS, meaning that the convolution alone does not lead to a complete spectral match between the instruments. To account for this and to minimize any remaining spectral features due to the difference in spectral resolutions, the differences between the CrIS spectra convolved with AIRS SRF and AIRS spectra are spectrally smoothed, particularly in the LW region. The effect of this spectral smoothing is shown in later figures. It should be noted that Motteler and Strow (2019) prescribe a more rigorous method of converting the spectral resolution of AIRS to CrIS. For this study which focuses on radiometric comparisons (broad spectral features) rather than spectral comparisons (single channel features), the aforementioned method is adequate.

### 3.3. High Latitude Comparisons

To perform a three-way comparison between each AIRS, IASI, and CrIS, the CrIS/AIRS SNOs are subset to a latitude range similar to that of the CrIS/IASI and AIRS/IASI SNOs—70° to 78° North for the Northern Hemisphere (NH) analysis and 70°–78° South for the Southern Hemisphere (SH) analysis. The time period from 1 October 2019 to 1 October 2020 is used to capture the recent current status of the AIRS, IASI, and CrIS comparisons over a whole year. Prior to this time period, IASI-A used a different nonlinearity correction. In addition to using the sounder radiance quality control flags, a simple quality control is applied to the SNO brightness temperature (BT) differences where differences with a magnitude greater than 20 K are excluded from the analyses. This screen is meant to remove potential outliers.

Whether the SNO difference spectra are either (a) averaged in radiance units and then converted to BT units, or (b) first converted to BT units and then averaged made a small but significant difference in the bias result. As an example, the SNPP CrIS and IASI-B weighted bias differed for most channels by a maximum of 0.01 K in the LW and MW, and 0.05 in the SW when the two different methods were used. A figure showing this effect is included in Figure S2 in Supporting Information S1. Figure S2 in Supporting Information S1 shows the numbers given above are for many channels a gross overestimate of what they actually are, especially for the spectrally smoothed result; however, this effect should not be completely dismissed. It is noted that the differences of Figure S2 in Supporting Information S1 have a magnitude that is similar to the sampling uncertainties which will be discussed later in Section 4. For the analyses shown in this paper, the SNO difference spectra were first converted to BT units and then averaged to obtain difference biases.

A last note is added here on the negligibility of residual view angle biases between the hyperspectral IR sounder footprints. An example single month (October 2022) analysis of SNOs between NOAA-20 CrIS and IASI-C shows that only the four closest-to-nadir fields of regard (FOR) are included in the big circle SNOs for each CrIS and IASI. This translates into satellite zenith angles that range between 0° and ~7°. When the average of the satellite view angles are taken over the complete example month for each IASI and CrIS, the difference between them is only 0.11°. Brief analysis with a radiative transfer model confirms this view angle bias to have negligible effect on the result shown in this paper—an over-estimated 0.5° view angle change from nadir results in a maximum of a 0.001 K change in BT across the full CrIS spectrum.

Figure S3 in Supporting Information S1 shows maps of the subset CrIS/AIRS, CrIS/IASI, and AIRS/IASI SNOs for this single year time period. Figures S4–S6 in Supporting Information S1 show histograms of the SNO

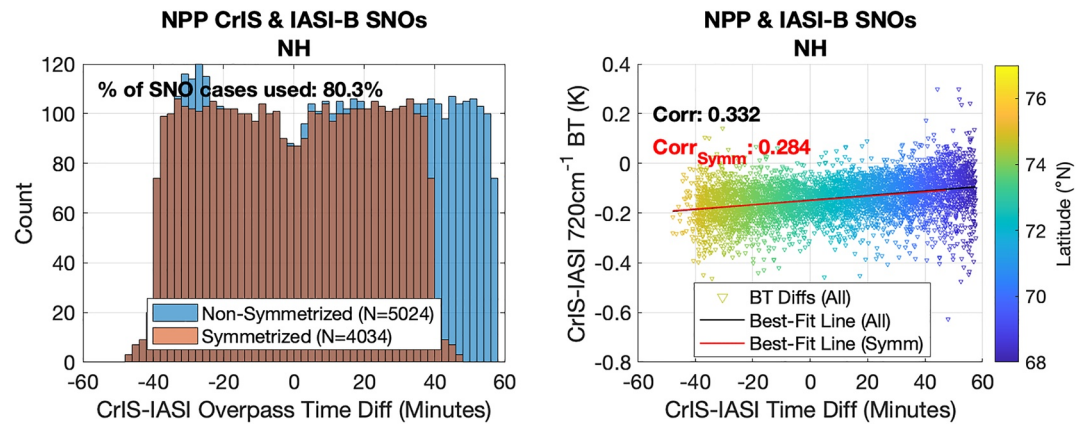


**Figure 1.** Simultaneous nadir overpasses (SNO) Time Difference Symmetrization: (left) symmetrized and non-symmetrized histograms of Suomi National Polar-Orbiting Partnership (SNPP) minus IASI-B overpass time differences for the Northern Hemisphere (NH) with the percent of SNO cases retained after symmetrization listed at the top; (right) SNPP and IASI-B  $720\text{ cm}^{-1}$  brightness temperature (BT) differences plotted against the CrIS minus IASI-B time difference for the NH colored by latitude overlaid by a best fit line with correlation of the  $720\text{ cm}^{-1}$  BT differences and time differences listed in the top left corner.

latitudes, longitudes, and overpass time differences. The similarity of these histograms enables comparison of the various SNO datasets.

### 3.4. Time Difference Symmetrization

One of the updated methods used in this study is the symmetrization of the overpass time difference histograms. For certain wavenumbers, namely the carbon dioxide absorption region, the CrIS/IASI and AIRS/IASI SNO BT differences can be slightly correlated with the difference between the satellite overpass times. An example of this correlation is illustrated in Figure 1 for SNPP CrIS and IASI-B for the  $720\text{ cm}^{-1}$  channel, where a correlation coefficient of 0.332 is seen between the overpass time difference and CrIS minus IASI BT differences. One hypothesis for this effect is the diurnal warming of the stratosphere. To remove any potential bias from this effect, a random selection of an equal number of samples from each side of the time difference histogram is made. This is facilitated using 2-min time difference bins. Figure 1 shows after this subsetting is made, the correlation between the BT differences and time differences drops to 0.284. Figure 1 also shows the CrIS-IASI time difference histogram before and after this random selection, or “symmetrization” of the histogram, is applied. For this particular case, using SNPP and IASI-B in the NH, about 80% of SNO samples are maintained after symmetrization. The other various platform combinations for CrIS/IASI and AIRS/IASI have similar yields, where between 70% and 82% of SNO samples are kept. Figure 1 shows the non-symmetrized time difference histogram is indeed skewed to one side so that if a mean was taken over the full data set, it could be expected to be affected by temporal sampling mismatch effects. This method is more important to use on the CrIS/IASI and AIRS/IASI data sets than the CrIS/AIRS data sets due to the fact that a much tighter time mismatch criterion can be applied to the CrIS/AIRS datasets due to the higher yield of SNO samples. Thus, this time symmetrization is not applied to the CrIS/AIRS data sets analyzed in Section 6. However, it is applied to the CrIS/AIRS subset of data used in Section 5 for similarity purposes.

## 4. Big Circle SNO Uncertainty Theory

A challenging but important aspect of comparing measurements from two instruments is ensuring the spatial and temporal mismatch is minimized and accounted for in an uncertainty estimate. The method adopted here is taken from Tobin et al. (2016) and Taylor et al. (2020), which discuss the theoretical uncertainties due to sampling differences between two satellite-based sounding instruments. The setup of the sounder comparisons they describe is somewhat different than the big-circle SNO method used here (defined previously in Section 3) but has an analogous comparison approach. In Tobin et al. (2016), a hypothetical reference sounder with large footprints (e.g.,  $\sim 100\text{ km}$  radius) is compared to currently existing high spectral resolution infrared sounders, for

**Table 1**  
*Typical Values of Parameters Used in the Simultaneous Nadir Overpass Spatial Sampling Uncertainty Equation for Each Combination of Cross-Track Infrared Sounder (CrIS), Atmospheric Infrared Sounder (AIRS), and Infrared Atmospheric Sounding Interferometer*

	CrIS and IASI	CrIS and AIRS	AIRS and IASI
Area of overlap (km <sup>2</sup> )	2,714.2	5,621.2	2,998.4
$O_{\text{CrIS}}$	17.6	36.5	–
$O_{\text{AIRS}}$	–	39.3	20.9
$O_{\text{IASI}}$	24.0	–	26.5
$M_{\text{CrIS}}$	111.9	66.0	–
$M_{\text{AIRS}}$	–	74.0	125.0
$M_{\text{IASI}}$	49.5	–	49.5

*Note.* To obtain the values in the table, averages were taken across the NH and SH as well as over instrument platform (i.e., for CrIS and AIRS parameters, values from NOAA-20 CrIS/AIRS and SNPP CrIS/AIRS were averaged together). Assumed radii for each CrIS, AIRS, and IASI footprints are noted in the text (See Section 3 for more details).

example, AIRS, IASI, or CrIS, which have smaller footprints with radii on the order of 10 km. With this setup, Tobin et al. (2016, Section 3.2.2) introduces the concepts and mathematical formulations for quantifying spatial and temporal sampling uncertainties between two sounding instruments. Taylor et al. (2020, Section 6) later iterated on the mathematical formulations laid out by Tobin et al. (2016) and provided an update with corrected limits as the number of smaller sounder footprints within the larger sounder footprint goes to zero or equals the number of effective footprints contained within the larger sized footprint.

Also described in these studies is a rigorous approach to computing weighted ensemble means of the Gaussian distributed instrument differences. In their approach, comparisons of lesser quality due to increased sampling differences between the instruments (e.g., in time or space) are down-weighted. In the formulation, weights are computed from the individual sampling uncertainties associated with each comparison and are then applied to the corresponding instrument differences before finding the mean difference value. Additionally, an uncertainty for the weighted bias, based on the sampling uncertainties, is included.

Analyses shown in this paper make use of the sampling uncertainty formulations described in the two previously mentioned studies. Equations are restated below in a form that is tailored to the big circle SNO method as described in the previous Section 3—specifically for two sounders with approximately equal sized footprints, some of which overlap. In this situation, the footprints from each instrument that fall within a “big circle” which has a defined radius and center location are used in the comparisons. With this setup, the effective number of footprints within the big circle that contribute no spatial sampling error because they overlap each other,  $O$ , needs to be defined for each instrument as:

$$O = A_{\text{overlap}} / A_{\text{footprint}}, \quad (1)$$

where  $A_{\text{overlap}}$  is the total area of overlap between the two sounders' footprints and  $A_{\text{footprint}}$  is the area of a single sounder footprint. Table 1 lists the average areas of overlap and  $O$  values for the instrument combinations shown in this paper. Here, the area of the instruments' footprints and overlaps are computed assuming that the footprints are perfect circles so that  $A_{\text{footprint}} = \pi R^2$ , where  $R$  is the radius of the footprint. The radii assigned to each instrument are chosen to be reflective of the radii values when the instruments are pointing at nadir. For CrIS this value is 7 km, for IASI it's 6 km, and for AIRS it's 6.75 km. For these SNO comparisons, which are restricted to near nadir view angles, these are valid approximations—e.g. only the four closest to nadir CrIS and IASI FOR are included in each SNO (i.e., FORs 14–17). Table 1 shows that the average area of footprint overlap for CrIS and AIRS is around 5,600 km<sup>2</sup>, which is ~90% larger than the AIRS and IASI overlap (which is ~2,998 km<sup>2</sup>) and over 100% larger than the CrIS and IASI overlap (which is ~2,714 km<sup>2</sup>). The area of overlap between CrIS and AIRS is larger than either CrIS or AIRS with IASI due to the sparser spatial sampling of IASI. The lower sample density of IASI also causes the CrIS/AIRS  $O$  values to be significantly different than the CrIS/IASI and AIRS/IASI values. Table 1 shows the average  $O$  values range from ~17 to 40 depending on the instrument combination being used.

Another term used to compute the spatial sampling uncertainty is the number of footprints from each sounder within the big circle, defined as  $M$ . Table 1 shows the average  $M$  values range from 50 to 125 depending on the instrument. For direct AIRS to CrIS comparisons, the AIRS  $M$  values are smaller than for the AIRS to IASI comparisons, because the big circle used in the AIRS to CrIS matchup is relatively smaller. These terms are then used in the following equation, which defines a spatial variance, used as the SNO spatial sampling uncertainty:

$$\sigma_{\text{space}}^2 = (1 - o_1/M_1)\sigma_1^2/M_1 + (1 - o_2/M_2)\sigma_2^2/M_2 \quad (2)$$

where  $\sigma$  is the standard deviation of the sounder measurements within the big circle. This equation is derived such that the mean measurement over the big circle for each instrument is thought of as an area weighting of samples which overlap and samples which do not overlap (Taylor et al., 2020). Note that if there is no overlap, the equation gives the expected sum of the uncertainty variance for two independent random variables, and if all of the footprints overlap, there is no sampling error.

Once the spatial sampling uncertainties are computed, and if all other sources of uncertainty are ignored or assumed negligible (e.g., temporal sampling or instrument noise), then the individual weights,  $w$ , are computed as:

$$w = 1/\sigma_{\text{space}}^2 \quad (3)$$

and the uncertainty for the ensemble weighted mean as (where  $N$  is total number of SNOs included in the ensemble mean):

$$u = \sqrt{1/\sum_{i=1:N} w_i} \quad (4)$$

In these analyses, we assume that the temporal sampling uncertainty is negligible for the ensemble mean. While there may be a small uncertainty from looking at slightly different atmospheres at different times, the use of the 60-min time difference criterion between overpass times aims to minimize this, in addition to the time difference histogram symmetrization detailed in Section 3.4. We also assume that the instrument noise is negligible when using the ensemble means. It can be noted that this last assumption may not be true if (a) there is still instrument noise leftover on the individual “big circle averages” (which indeed is true for very cold scenes) and (b) if the weights computed from the sampling uncertainty have extreme outlying values that weight a few single spectra much more heavily than the rest. That is, some big circle average spectra which still have residual noise in them could get weighted heavily enough in the ensemble mean that the noise associated with those spectra gets propagated through the averaging. We note this as a caveat and potential obstacle of the method we employ, but we do not believe this is happening in the analyses included in this paper due to inspection of the distribution of individual weights applied in each analysis.

## 5. High Latitude SNO Comparisons

This section shows results from the comparison of SNOs at the high latitudes. The CrIS/AIRS SNOs here have been subset to be at coincident latitudes as the CrIS/IASI and AIRS/IASI SNOs.

### 5.1. CrIS and IASI

Results for CrIS and IASI SNO comparisons are shown in Figures 2 and 3 for SNPP CrIS and NOAA-20 CrIS respectively. The weighted biases for each CrIS against METOP-A, -B, and -C IASI are shown overlaid with the corresponding spatial sampling uncertainties. The sampling uncertainties as shown in these Figures are indistinguishable from the biases on the scales used, as they are less than 0.03 K  $3\sigma$  across the full spectrum for each SNPP and NOAA-20 comparisons, often being much less than 0.03 K. Spectrally smoothed versions of the biases are produced via application of a hamming apodization to reveal potential broader spectral features produced by radiometric calibration errors as well as to represent the form of the CrIS data which is currently used by major numerical weather prediction centers. Lastly, the  $3\sigma$  CrIS RU is shown in the bottom panels of Figures 2 and 3, which for this subset of dominantly cold scene data is less than 0.15 K across the full spectrum for each CrIS sensor. It is noted that this uncertainty is representative of the systematic component only and is taken from the NASA CrIS L1b Version 3 product (UW-Madison, 2022).

Spectrally smoothed CrIS minus IASI biases are generally less than 0.25 K (LW), 0.1 K (MW), and 0.15 K (SW). In general, the CrIS-IASI biases for each METOP-A, -B, and -C are tightly grouped together. Close inspection of the CrIS-IASI biases in the LW reveals that the biases from METOP-A and METOP-C are closer to each other than to the bias from METOP-B at wavenumbers less than 700  $\text{cm}^{-1}$ . This behavior has been seen in alternative analyses done by other groups as well (Barbier et al., 2021).

While primarily spectrally flat, the non-smoothed CrIS minus IASI bias contains some spectral regions of higher frequency bias features that are larger than their surrounding regions. For example, the 720–750  $\text{cm}^{-1}$  region has biases which have amplitudes of over 0.05 K. Analysis suggests that this larger bias region in particular is not due to a spectral calibration issue; other possible sources for this error are CrIS nonlinearity, IASI nonlinearity, or small view angle differences between the instruments. This region is highlighted due to its important role in temperature sounding of the atmosphere. The large bias feature visible in the SNPP SW region around 2,370  $\text{cm}^{-1}$  is not due to either CrIS or IASI having gross calibration issues but is caused by the highly sensitive conversion from radiance units to BT units at very small radiance values at this wavenumber. Overall consistency is seen between results from the Northern and SH, and where differences exist, they are due to the difference



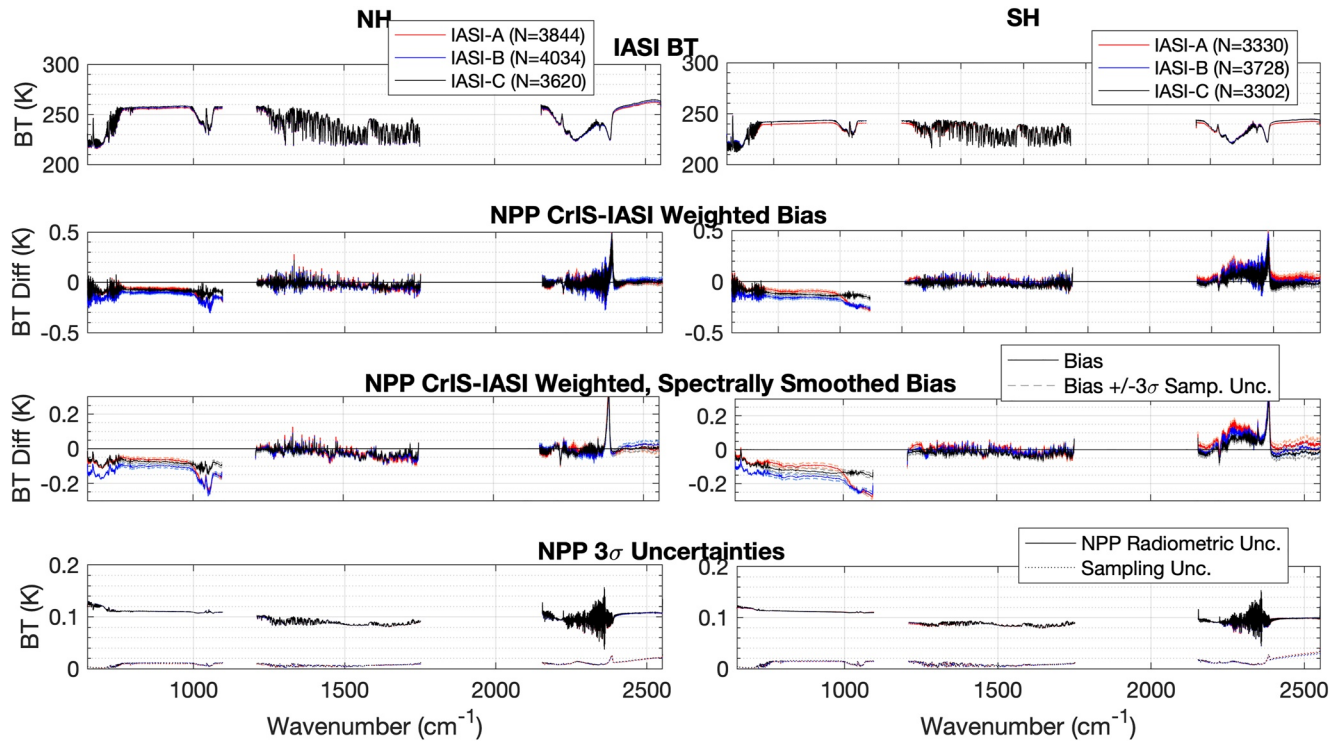


**Figure 2.** Suomi National Polar-Orbiting Partnership (SNPP) Cross-track Infrared Sounder (CrIS) and Infrared Atmospheric Sounding Interferometer (IASI)-A/B/C simultaneous nadir overpass comparisons. Northern Hemisphere (left column) and Southern Hemisphere (right column) results for (top) the average IASI brightness temperature, (second from top) the weighted SNPP CrIS-IASI bias with  $3\sigma$  spatial sampling uncertainty, (second from bottom) the weighted and spectrally smoothed SNPP CrIS-IASI bias with  $3\sigma$  spatial sampling uncertainty, and (bottom) the estimated  $3\sigma$  CrIS radiometric uncertainty and  $3\sigma$  sampling uncertainty. Note the biases plus or minus the  $3\sigma$  sampling uncertainty are not distinguishable from one another on the given axis scales.

in scene temperature. Differences between the two CrIS instruments using IASI as a common reference are presented in Section 5.4.

## 5.2. AIRS and IASI

Figure 4 shows the comparison of AIRS and IASI-B for the NH and highlights the detector characteristics of the AIRS instrument. Vertical dotted lines demarcate the transition between AIRS linear detector arrays and marker styles indicate what combination of AIRS detectors are used—A or B detectors. Some detector arrays have identifiably different bias characteristics than others, for example, larger channel-to-channel variation or larger bias offsets from zero, but most transitions from one array to another array are spectrally smooth. The combination of which A or B detectors are used for each reported channel does not seem to impact the bias characteristics. This is an improvement upon previous AIRS calibration versions where A and B detectors had very different behaviors in select detector arrays (Tobin et al., 2006). In general, Figure 4 shows that for most spectral regions, AIRS detector characteristics play a minimal role in the AIRS-IASI bias characteristics.

Figure 5 shows all AIRS and IASI comparisons for both the NH and SH. AIRS minus IASI weighted biases for each METOP-A, METOP-B, and METOP-C are overlaid in the middle panel, and analogous spectrally smoothed biases are shown in the bottom panel. The application of spectral smoothing reveals the broader spectral features caused by radiometric calibration errors, while the non-smoothed version can highlight errors due to spectral calibration issues (due to the close to exact spectral resolution conversion for this pair of sensors). Also plotted are the  $3\sigma$  bias sampling uncertainties which are less than approximately 0.02 K across the full spectral range of the measurements (not distinguishable from biases on given y-scale). As for the CrIS minus IASI biases, readily apparent is that AIRS minus IASI biases for each METOP-A, -B, and -C give very similar results, highlighting the consistency among the three IASI instruments. The AIRS-IASI smoothed biases are generally under 0.3, 0.25, and 0.15 K for the LW, MW, and SW respectively. While in some regions the biases are spectrally flat on the scale shown, such as the SW and LW windows, larger areas of disagreement between AIRS and IASI do exist, for example, around 700, 1,050  $\text{cm}^{-1}$  and

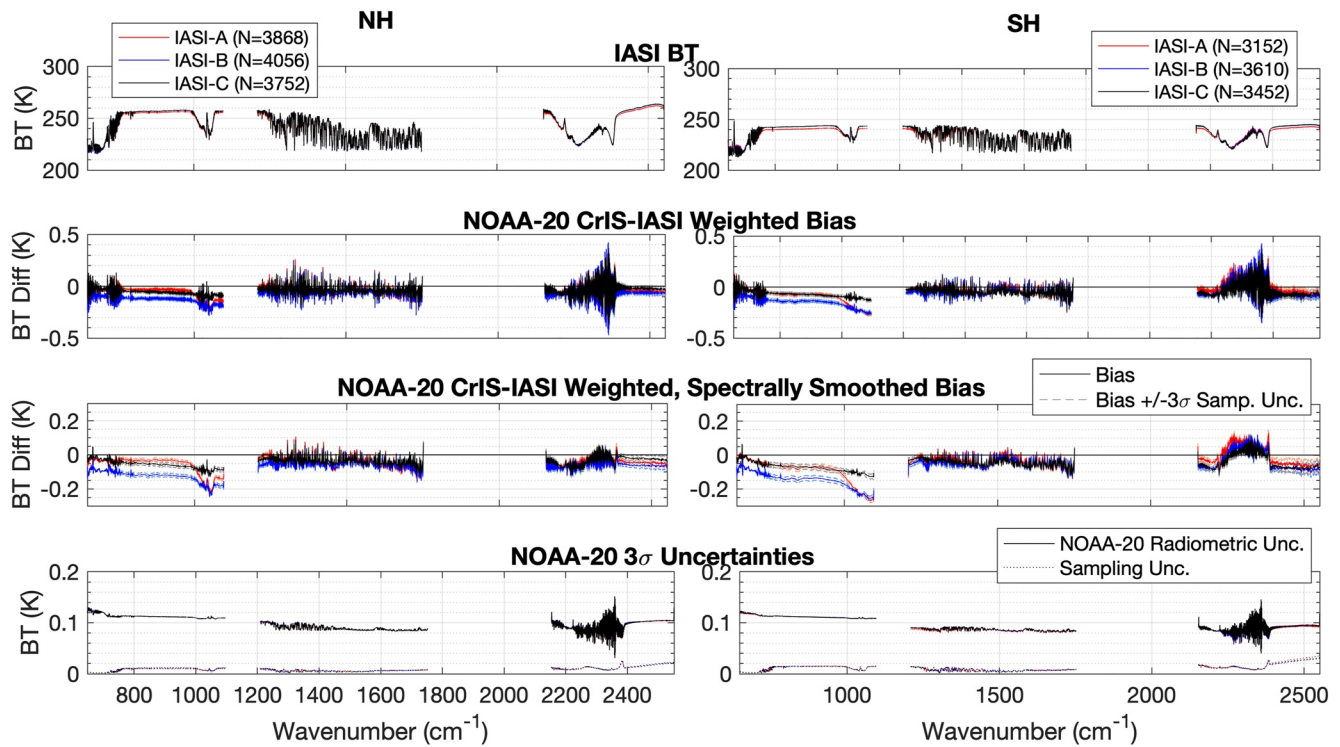


**Figure 3.** NOAA-20 Cross-track Infrared Sounder (CrIS) and Infrared Atmospheric Sounding Interferometer-A/B/C simultaneous nadir overpass comparisons. Same as Figure 2 except for NOAA-20 CrIS.

1,500–1,600  $\text{cm}^{-1}$ . The tight agreement of the IASI instruments in these regions (using AIRS as a reference) suggests AIRS has calibration errors in these regions. This is further evidenced by comparisons with CrIS in Figures 2 and 3.

### 5.3. CrIS and AIRS

Figure 6 shows differences between AIRS and the two CrIS instruments via SNOs. Here it is important to note again that the CrIS FSR product which is convolved with the AIRS SRFs does not fully match the AIRS resolution, particularly in the LW band. This is because AIRS has some contribution from large optical path differences

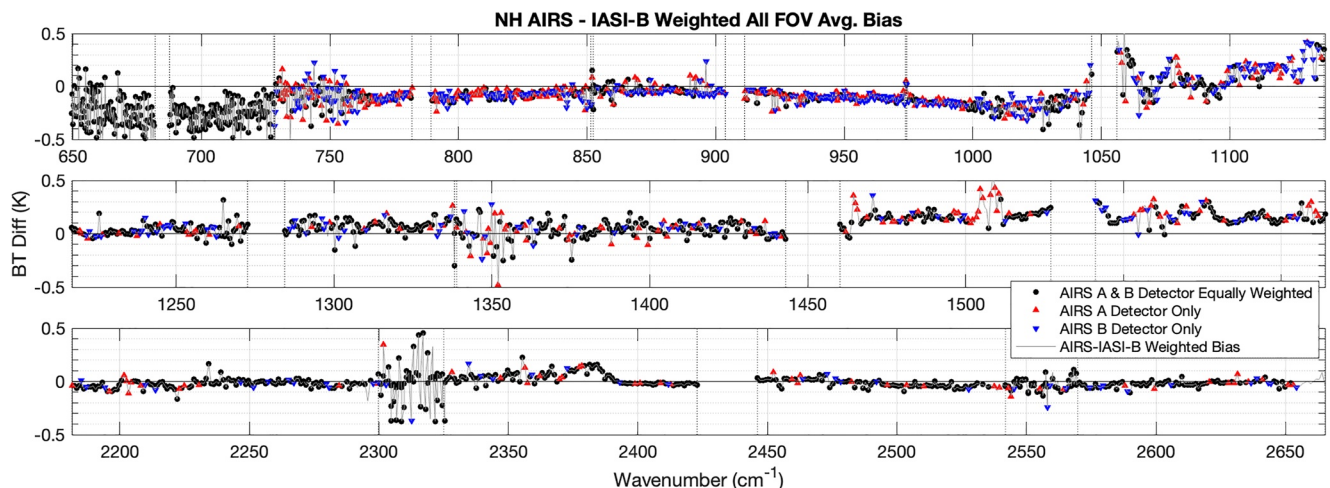


**Figure 4.** Atmospheric Infrared Sounder (AIRS) and Infrared Atmospheric Sounding Interferometer (IASI)-B simultaneous nadir overpass comparison illustrating the AIRS detectors characteristics. Vertical dashed lines denote transitions between the AIRS detector arrays. Marker styles indicate whether the AIRS channel used data from the “A” or “B” detector or a combination of “A” and “B.” The bias shown is the AIRS minus IASI-B Northern Hemisphere weighted bias.

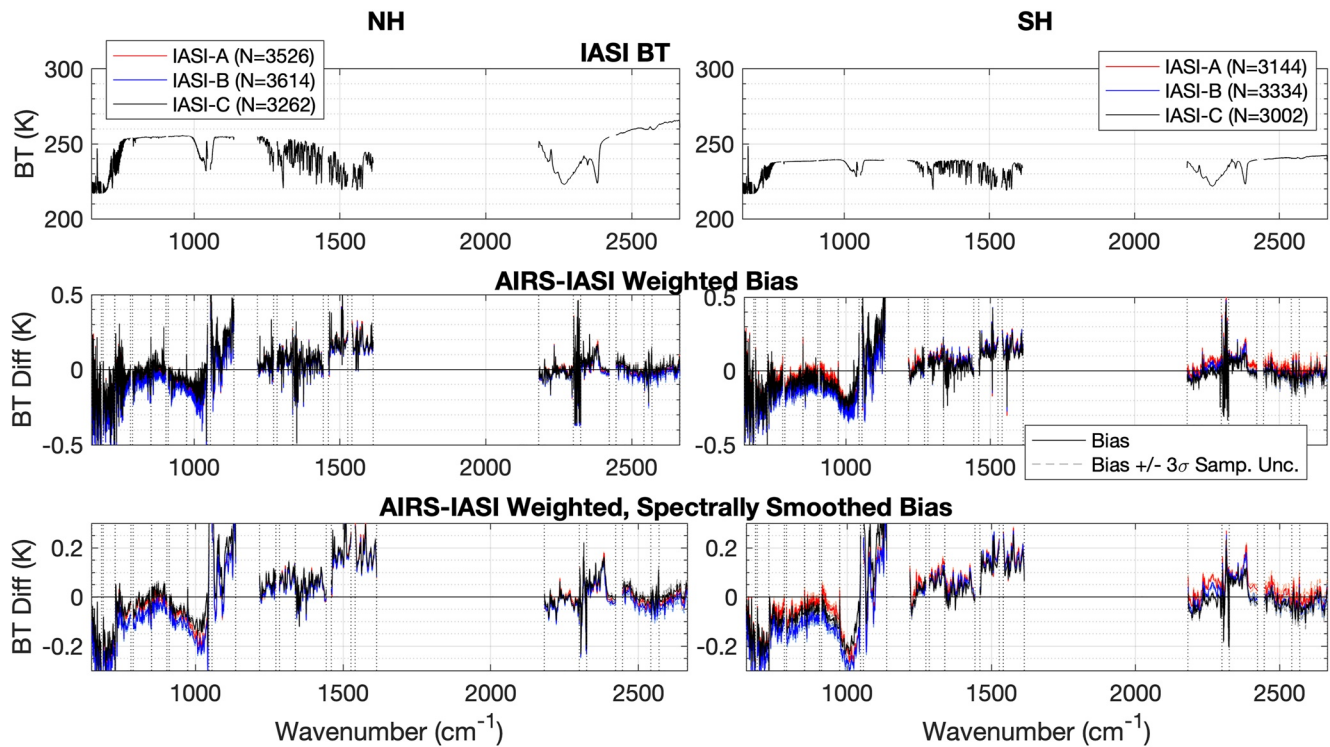


**Figure 5.** Atmospheric Infrared Sounder (AIRS) and Infrared Atmospheric Sounding Interferometer (IASI)-A/B/C simultaneous nadir overpass comparisons. Northern Hemisphere (left column) and Southern Hemisphere (right column) results for (top) the average IASI brightness temperature, (middle) the weighted AIRS minus IASI bias with  $3\sigma$  spatial sampling uncertainty, and (bottom) the weighted and spectrally smoothed AIRS minus IASI bias with  $3\sigma$  spatial sampling uncertainty. Note the biases plus or minus the  $3\sigma$  sampling uncertainty are not distinguishable from one another on the given axis scales.

(delays) not sampled by CrIS, even though CrIS has effectively higher spectral resolution in the  $670\text{ cm}^{-1}$  region. Thus, the non-smoothed result, shown in Figure 6 (second panel from the top), does not show an exact spectral match between the instruments in the LW and the LW fine scale spectral features should not be interpreted as “real” differences—the result is only shown as an illustration of what the differences look like. The spectral smoothing applied to the biases (shown in the second panel from the bottom) serves to remove higher resolution spectral features due to spectral resolution differences and to reveal the broader spectral scale features associated with radiometric differences.

When spectrally smoothed, it is apparent that the bias between SNPP CrIS and AIRS and the bias between NOAA-20 CrIS and AIRS are qualitatively similar and have the same spectral difference signatures. The sampling uncertainties associated with the biases are less than  $0.02\text{ K } 3\sigma$ , and the CrIS radiometric uncertainties for each SNPP and NOAA-20 are less than  $0.15\text{ K } 3\sigma$  across the spectrum for each the NH and SH. Regions of larger biases between CrIS and AIRS (for each the NH and SH) exist around  $700$ ,  $1,050\text{ cm}^{-1}$  and  $1,500\text{--}1,600\text{ cm}^{-1}$ . When compared to the biases from IASI and AIRS, similarities are seen, implying that AIRS calibration errors are causing the larger, broader spectral signatures in the biases against CrIS or IASI. Note that in Figure 6 the difference is CrIS minus AIRS whereas in Figure 5 the difference is AIRS minus IASI. This causes a sign change in the bias between these two figures.

#### 5.4. NOAA-20 CrIS Minus SNPP CrIS Double Difference

Analysis in Figure 7 shows the NOAA-20 minus SNPP CrIS double differences computed using the spectrally smoothed CrIS-IASI and CrIS-AIRS biases presented in the previous subsections. Confidence can be had in this double difference result because, for the given time period, the NOAA-20 CrIS SNOs and SNPP CrIS SNOs with AIRS and IASI have very similar scene temperature distributions and mean values. Corresponding spatial sampling uncertainties and CrIS radiometric uncertainties are computed via a root sum square (RSS) of the uncertainties from each individual SNO bias. The CrIS radiometric uncertainties for each the NH and SH double

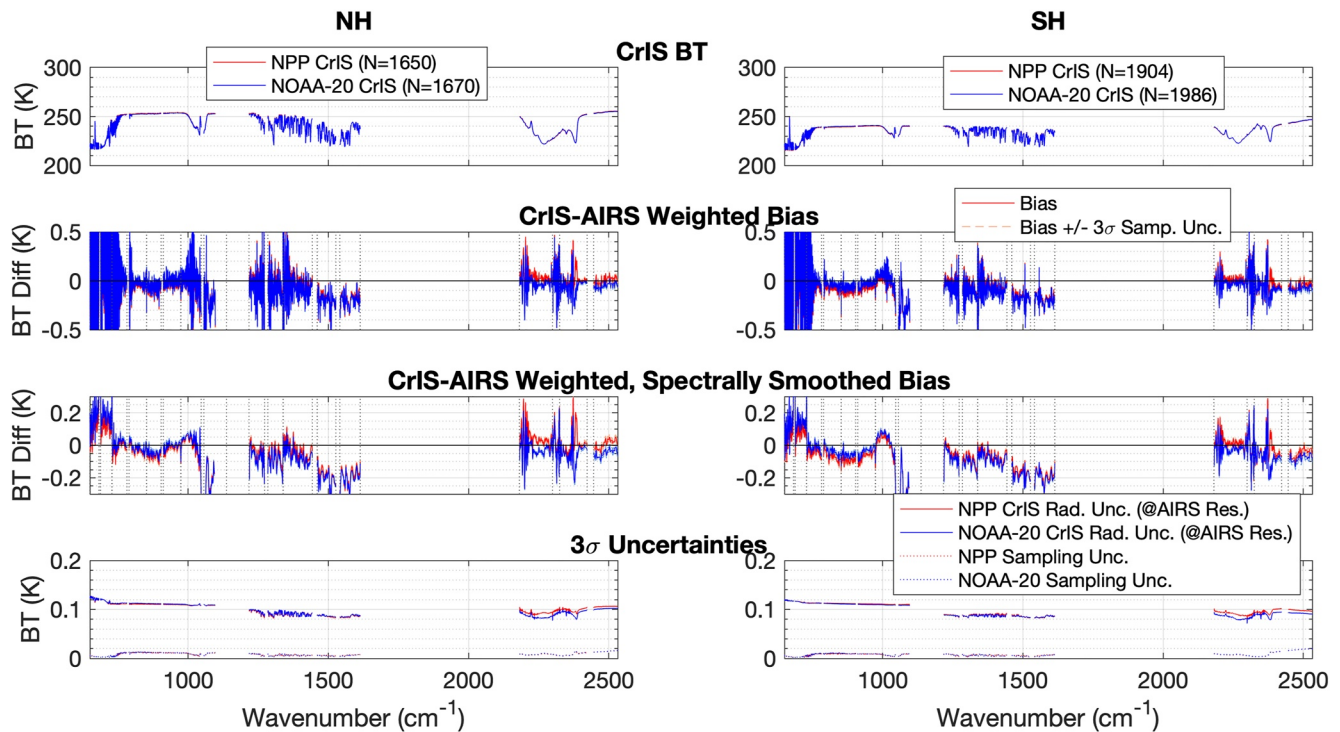


**Figure 6.** Suomi National Polar-Orbiting Partnership/NOAA-20 Cross-track Infrared Sounder (CrIS) and Atmospheric Infrared Sounder (AIRS) simultaneous nadir overpass comparisons. Northern Hemisphere (left column) and Southern Hemisphere (right column) results for (top) the average CrIS brightness temperature, (second from top) the weighted NOAA-20 CrIS minus Infrared Atmospheric Sounding Interferometer (IASI) bias  $\pm 3\sigma$  spatial sampling uncertainty, (third from top) the weighted and spectrally smoothed NOAA-20 CrIS minus IASI bias  $\pm 3\sigma$  spatial sampling uncertainty, and (bottom) the  $3\sigma$  CrIS radiometric uncertainty and  $3\sigma$  sampling uncertainty. Please note the non-smoothed results do not represent an exact spectral match between the AIRS and CrIS instrument (see text for further description). The biases plus or minus the  $3\sigma$  sampling uncertainty are not distinguishable from one another on the given axis scales.

difference are under 0.2 K, while the spatial sampling uncertainties are generally under  $\sim 0.02$  K in the LW/MW and 0.04 K in the SW.

The CrIS double differences estimated using AIRS and those estimated using each IASI are qualitatively similar with similar spectral structures and similar orders of magnitude. This is true for the NH and SH and provides confidence in the double difference results. The differences, being predominantly under 75 mK in the LW/MW

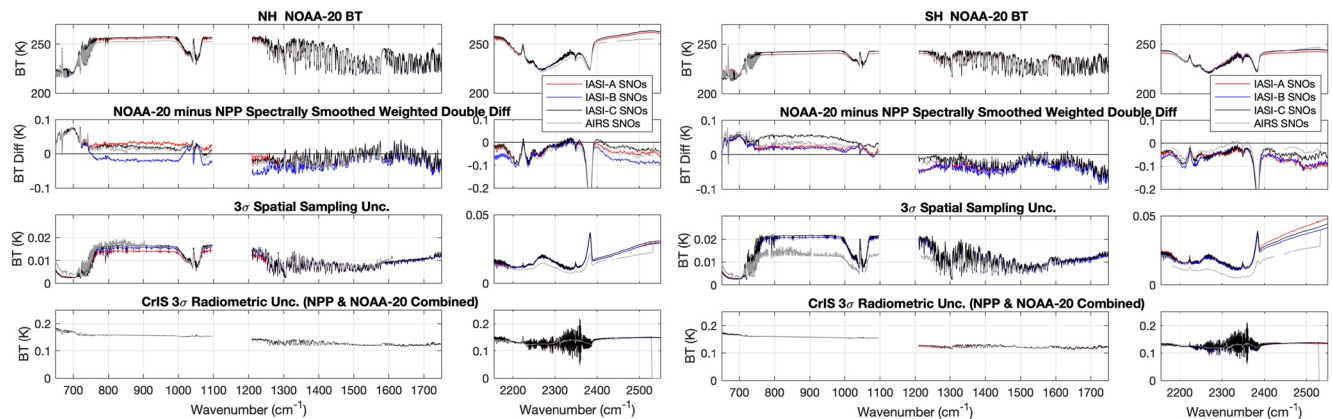


**Figure 7.** NOAA-20 minus Suomi National Polar-Orbiting Partnership (SNPP) Cross-track Infrared Sounder (CrIS) double differences via Atmospheric Infrared Sounder and Infrared Atmospheric Sounding Interferometer-A/B/C. Northern Hemisphere (left) and Southern Hemisphere (right) results for (top) the average NOAA-20 CrIS brightness temperature, (second from top) the weighted, spectrally smoothed NOAA-20 CrIS minus SNPP CrIS double difference, (second from bottom) the corresponding  $3\sigma$  spatial sampling uncertainty, and (bottom) the  $3\sigma$  combined SNPP and NOAA-20 radiometric uncertainty.

and predominantly under 100 mK in the SW, are overall smaller than the  $3\sigma$  CrIS RU (with an exception for the  $2,370\text{ cm}^{-1}$  region where conversion to BT units causes artifacts). Thus, across most of the spectrum the SNPP and NOAA-20 CrIS instruments are in statistical agreement. This result is consistent with a similar recent analysis performed by Strow et al. (2021).

The spatial sampling uncertainty is much smaller than the CrIS combined radiometric uncertainties, again, being under 0.02 K for the majority of the LW and MW bands and under 0.04 K for most of the SW band. Despite the extremely small values of the CrIS double differences, the SNO  $3\sigma$  sampling uncertainties are still notably smaller than the differences in some spectral regions, for example, the LW  $650\text{--}700\text{ cm}^{-1}$  region where the sampling uncertainty is a full order of magnitude smaller than the NOAA-20 minus SNPP CrIS differences. In this spectral region in particular, the CrIS double difference estimates via AIRS and each IASI are all very close together overlaying each other on the plot. The fact that the sampling uncertainty is smaller than the CrIS double difference implies that the SNO methodology employed is a sophisticated enough matching tool to be able to inform about where the instruments could be in better agreement. That is, while the two CrISes are already in statistical agreement according to their radiometric measurement uncertainties, the sampling uncertainties inform that the measurements could still be more consistent. This tool could thus be useful in efforts to make the series of CrIS instruments more consistent with each other, something desirable for climate analyses. For example, the bias between the two CrIS instruments in the  $650\text{--}700\text{ cm}^{-1}$  and ozone absorption region around  $1,050\text{ cm}^{-1}$  has been hypothesized to be due to non-optimal nonlinearity correction on one or both CrIS instruments—thus the nonlinearity coefficients could be refined further within the respective uncertainties to address this to make the instruments more consistent.

### 5.5. Three-Way Comparison of AIRS, NOAA-20 CrIS, and IASI-C

Figure 8 shows a three-way comparison between NOAA-20 CrIS, AIRS, and IASI-C. The spectrally smoothed biases between each of these three instruments are shown overlaid in the second from the top panels of the figure. For both the NH and SH, sampling uncertainties again are generally less than 0.02 K across the spectrum and CrIS radiometric uncertainties are less than 0.15 K. The results from the NH and SH are overall similar. Both show that the IASI-C minus AIRS and NOAA-20 CrIS minus AIRS biases are qualitatively similar while the NOAA-20 CrIS minus IASI-C bias is much more spectrally flat. This implies again that AIRS has calibration errors in specific regions, for example, around  $700$  and  $1,500\text{ cm}^{-1}$ . When accounting for the NOAA-20 CrIS RU, NOAA-20 CrIS and IASI-C are in good general agreement when spectrally smoothed, and NOAA-20 CrIS and AIRS are often in disagreement greater than the CrIS  $3\sigma$  uncertainty. However, estimates of the AIRS measurement uncertainty from Pagano et al. (2020) suggest that AIRS does agree with CrIS and IASI within the respective instrument's combined measurement uncertainties. This example demonstrates the importance of using estimated on-orbit radiometric uncertainties when evaluating radiometric biases between sensors. While these differences between the three sounders are indeed small, they are still concerning for climate trending applications and highlight the need of a reference infrared sounder.

### 5.6. Brightness Temperature Dependence of SNO Biases

The dependence of the SNO BT differences on scene BT is shown in Figure 9 for various wavenumber ranges for each CrIS with AIRS and IASI-C. Biases are computed for 5-degree BT bins and have the spatial sampling uncertainty overlaid in dark colored error bars and the CrIS RU overlaid in light colored error bars. Note that RU estimates were not included for AIRS or IASI observations since they are not available for each sounding. This limits the interpretation to whether the observed bias between sensors can be explained by a RU in the CrIS sensor alone. For all wavenumber regions, which span each of the LW, MW, and SW detectors of CrIS and IASI, there is a small dependence on scene temperature. For the  $670\text{--}680\text{ cm}^{-1}$  spectral region, differences are less than 0.4 K in magnitude and the slight change of the bias with scene temperature is likely explained by the uncertainty of non-linearity corrections of each CrIS, IASI, and AIRS. The  $830\text{--}840\text{ cm}^{-1}$  window region biases, where not affected by small sample sizes (i.e., at scene temperatures less than 290 K), are generally not statistically significant and are less than 0.2 K in magnitude. In the MW  $1,382\text{--}1,407\text{ cm}^{-1}$  water vapor region the biases are less than 0.1 K magnitude at scene temperatures down to 225 K. In the  $1,585\text{--}1,600\text{ cm}^{-1}$  region the biases are less than 0.3 K magnitude down to 225 K, and both CrIS-AIRS biases show a statistically significant difference which is larger at colder scene temperatures; note the CrIS and AIRS SNOs also have smaller sampling

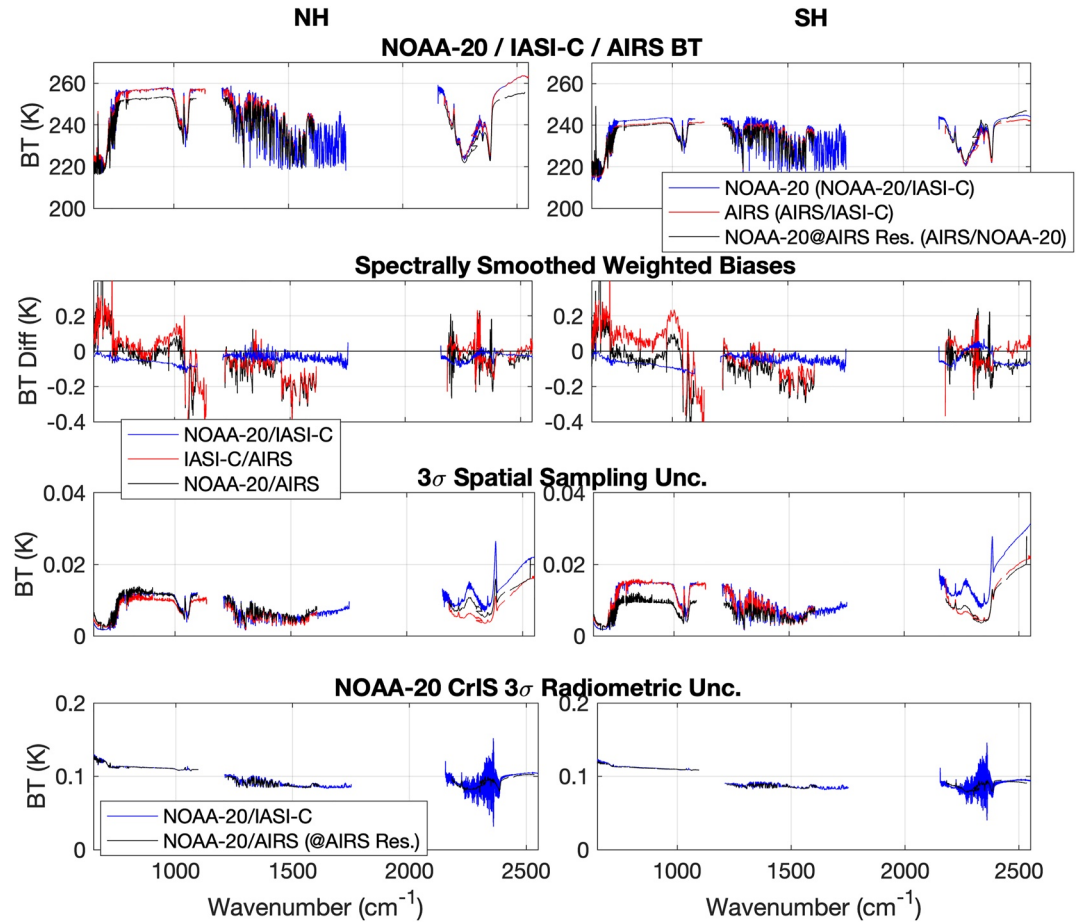


**Figure 8.** Three-way comparisons of NOAA-20 Cross-track Infrared Sounder (CrIS), Infrared Atmospheric Sounding Interferometer-C, and Atmospheric Infrared Sounder. Northern Hemisphere (left) and Southern Hemisphere (right) results are shown for the (top) mean brightness temperature, (second from top) spectrally smoothed biases, (second from bottom)  $3\sigma$  sampling uncertainty, and (bottom) NOAA-20 CrIS  $3\sigma$  radiometric uncertainty.

uncertainties than the CrIS and AIRS and IASI SNOs specifically at colder temperatures. For the SW  $2,360\text{--}2,370\text{ cm}^{-1}$  and  $2,500\text{--}2,520\text{ cm}^{-1}$  window region, the biases are overall not statistically significant.

Figure 10 shows the NOAA-20 CrIS minus SNPP CrIS double difference dependence on scene temperature for the same six wavenumber regions shown in Figure 9. Again, the  $3\sigma$  sampling and  $3\sigma$  CrIS RU are combined via RSS and shown with the bias. Overall, for each of the wavenumber regions, the CrIS double difference is less than the  $3\sigma$  CrIS RU—showing that the two CrIS instruments agree in a statistically meaningful way across most scene temperatures. Note that in this double difference any radiometric error in the reference (AIRS or IASI), cancels out and therefore the CrIS RU is the dominant contribution. Additionally, within the statistical sampling uncertainty NOAA-20 and SNPP CrIS, when compared using each IASI and AIRS, have very similar dependences on BT (very little if any). The CrIS double difference bias is less than 0.1 K for all scene temperatures at  $672\text{ to }681\text{ cm}^{-1}$  and is less than 0.1 K for both MW wavenumber regions where the result is not ill-affected by low number of samples (at scene temperatures greater than 225 K). In the remaining wavenumber regions, biases are largely less than 0.2 K.

## 6. CrIS and AIRS SNO Orbit Phase Dependence

In this study we use a complete year of data (1 October 2019–30 September 2020) to estimate the systematic bias between CrIS and AIRS as a function of orbit phase. Note that the prior sections of this paper only characterize the CrIS and AIRS differences for a narrow latitude band at high latitudes (see Supporting Information S1

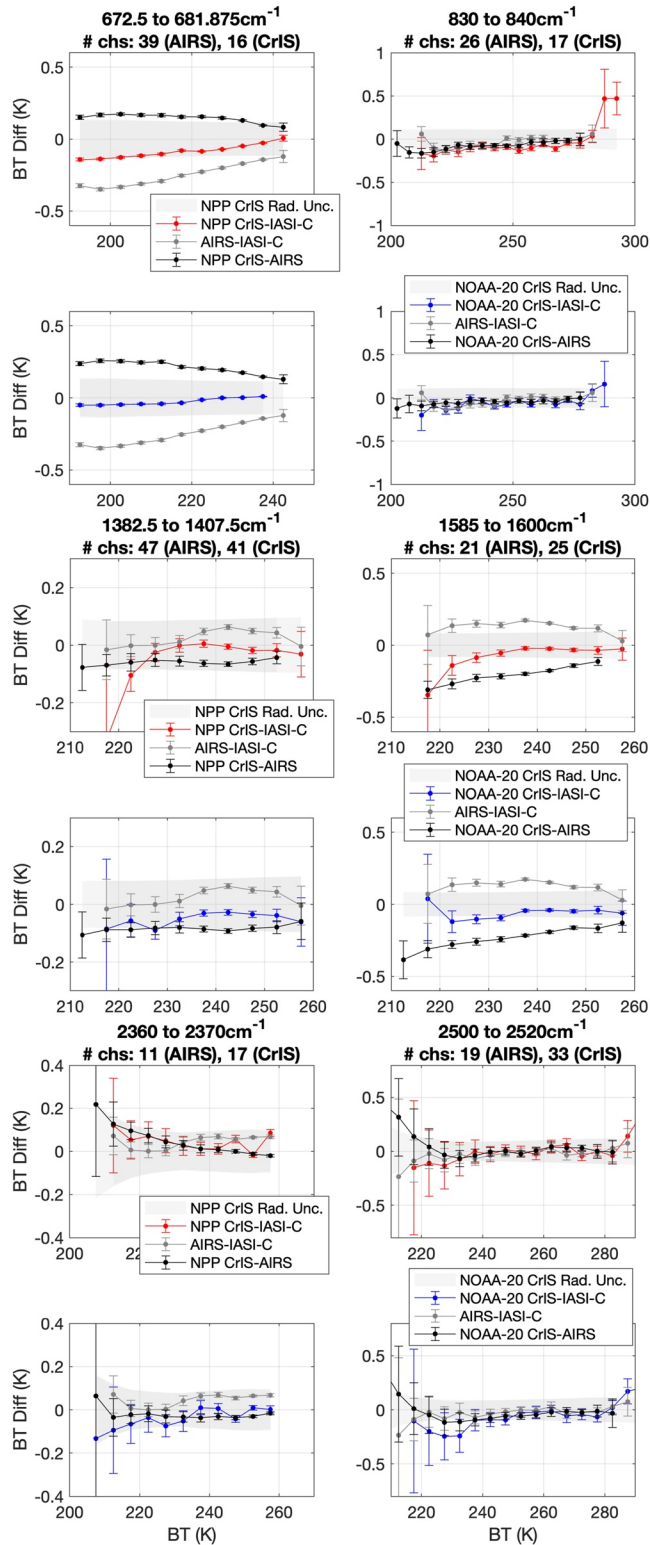


**Figure 9.** Dependence of Cross-track Infrared Sounder (CrIS), Atmospheric Infrared Sounder (AIRS), and Infrared Atmospheric Sounding Interferometer (IASI)-C simultaneous nadir overpass (SNO) differences on scene brightness temperature (BT). SNO biases are computed over 5-degree brightness temperature bins and are shown overlaid with their 3σ spatial sampling uncertainty in dark error bars and the CrIS 3σ radiometric uncertainty in light colored error bars. Results for the Northern Hemisphere and Southern Hemisphere are combined and are shown for six different wavenumber regions spanning the CrIS LW, MW, and SW detectors.

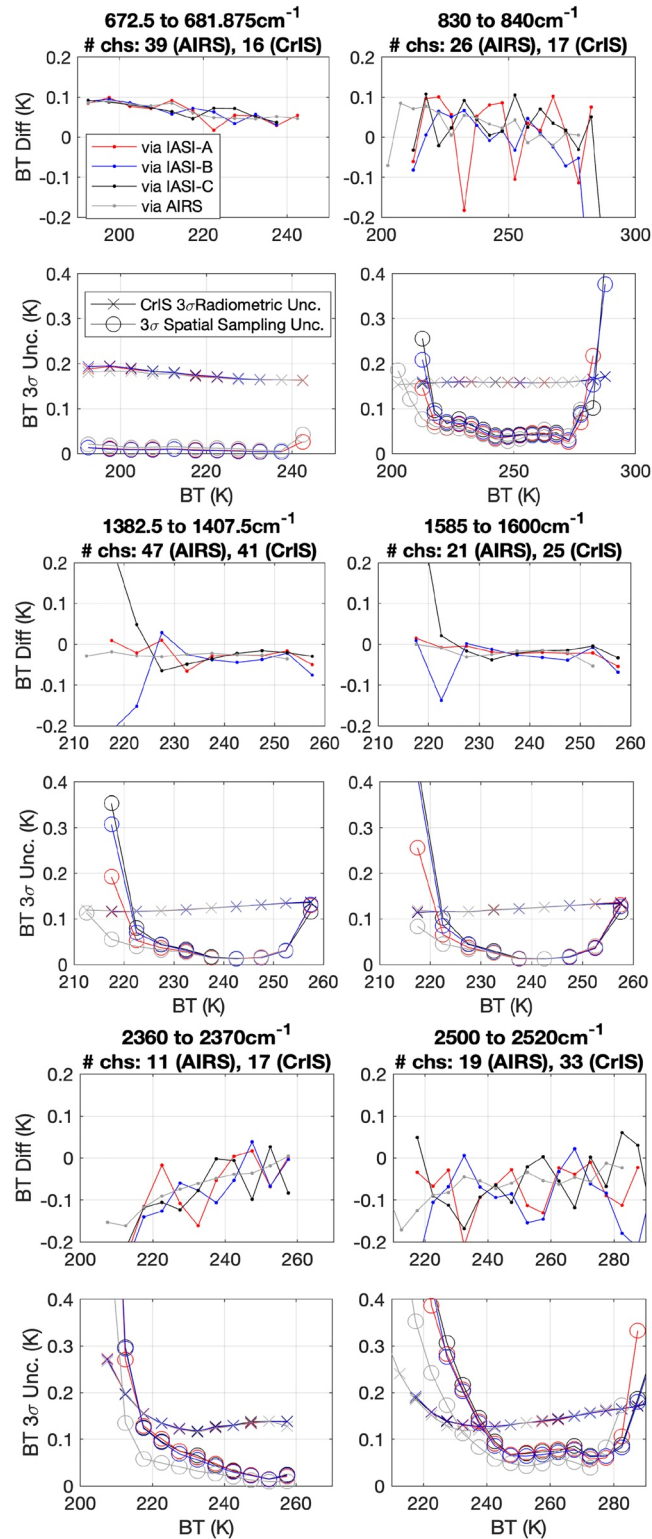


**Figure 10.** Dependence of the Cross-track Infrared Sounder (CrIS) double differences on scene brightness temperature. NOAA-20 minus Suomi National Polar-Orbiting Partnership CrIS double differences computed over 5-degree scene temperature bins are shown for the Northern Hemisphere and Southern Hemisphere combined (top panels). The  $3\sigma$  spatial sampling uncertainty and CrIS  $3\sigma$  radiometric uncertainty are also shown overlaid (bottom panels). Results are shown for six different wavenumber regions spanning the CrIS LW, MW, and SW detectors.



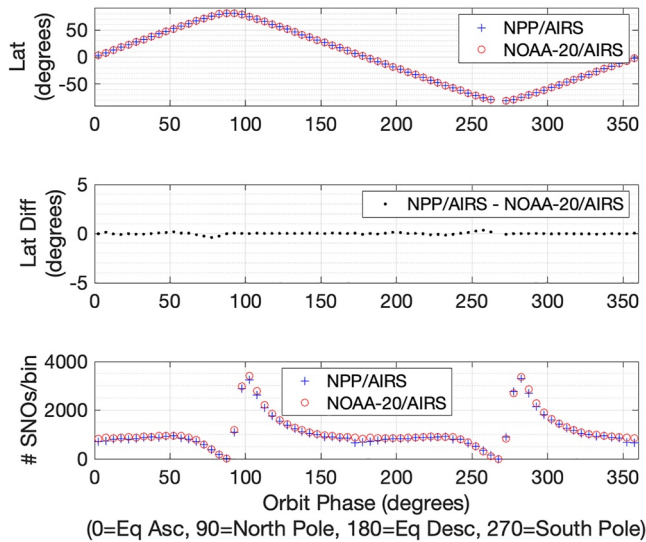


**Figure 11.** CrIS orbit phase dependence of global Cross-track Infrared Sounder (CrIS)/Atmospheric Infrared Sounder (AIRS) simultaneous nadir overpasses (SNOs). The average latitude (top panel), the mean latitude difference between the Suomi National Polar-Orbiting Partnership (SNPP) CrIS/AIRS and NOAA-20 CrIS/AIRS SNOs that fall within each bin (middle panel), and the number of SNOs in each bin for each SNPP CrIS/AIRS and NOAA-20 CrIS/AIRS (bottom panel).

for maps) and that for all analysis shown in this paper, no filtering on the solar zenith angle is applied. The characterization by orbit phase shown in this section includes a much wider range of Earth scene temperatures from equator to pole. Note however that the AIRS/CrIS SNOs are not distributed uniformly in latitude nor in longitude. A characteristic of the 16-day repeat cycle of the CrIS spatial sampling is that only a limited range of longitudes is sampled with the AIRS/CrIS SNOs and those same regions repeat throughout the calendar year. The AIRS/CrIS SNOs occur all along the CrIS orbit phase ( $0^{\circ}$ – $360^{\circ}$ ) but with variable sampling statistics along the orbit; in particular there is a higher number of SNOs in certain high latitude zones. Figure 11 illustrates this by showing the number of SNO samples by CrIS orbit phase, where the orbit phase is defined to be the angle from the center of the orbit to the satellite position relative to the ascending equator crossing. Specifically, Figure 11 shows for  $5^{\circ}$  orbit phase bins the (a) average latitude (b) mean latitude difference between AIRS and CrIS SNOs, and (c) the number of SNOs.

Figure 12 shows the orbit phase dependence of the SNPP and NOAA-20 CrIS SNOs with respect to AIRS for six different wavenumbers. For this analysis, the spectrally manipulated radiances are used (as described in Section 3.2). A dependence upon the orbital phase is seen in the mean BT and is largest for the surface sensing channels like  $900$  and  $2,500\text{ cm}^{-1}$ . Orbit phase dependency is also seen in both the SNPP CrIS-AIRS and NOAA-20 CrIS-AIRS differences, most notably in the SW channels where the differences vary by  $0.4\text{ K}$  across the orbit phase, reaching a maximum value of  $\sim 0.3\text{ K}$ . Error bars shown on the CrIS-AIRS difference represent the statistical uncertainty of the mean within a  $5^{\circ}$  orbital phase bin, that is, the standard deviation of the

individual SNO differences divided by the square root of the number of samples. The uncertainty values shown in Figure 12 are  $3\sigma$ . The very small error bars imply that nearly all the variability in CrIS-AIRS bias along the orbit phase is statistically significant.

The structures of the orbital phase dependency for SNPP and NOAA-20 CrIS-AIRS differences are largely similar to each other in the MW and SW channels but are slightly different for the LW channels. This is highlighted by the double difference results in Figure 12 which show SNPP CrIS minus NOAA-20 CrIS using AIRS as a reference. The CrIS double difference has an orbital dependence which is most obvious in the LW channels at  $680$  and  $900\text{ cm}^{-1}$ . Across all wavenumbers shown, the CrIS double difference has a maximum value of  $\sim 0.15\text{ K}$  and varies by about  $\sim 0.15\text{ K}$  over the orbit. The orbital variations of the SNPP CrIS minus NOAA-20 CrIS obtained using AIRS as a common reference warrant further investigation.

## 7. Conclusions

This section summarizes the analysis and findings of this paper, offers implications of the results, and points to areas of future work for the community.

New in this paper, to the historically performed high spectral resolution IR sounder SNO comparisons, was the use of spatial sampling uncertainties as outlined in Tobin et al. (2016) and Taylor et al. (2020) and modified here. These uncertainties quantify how well the various IR sounders can be compared using the SNO methodology. The inclusion of these uncertainties enables the claim of statistical statements; for certain spectral regions, the SNO biases are an order of magnitude larger than the sampling uncertainties. Also new to this paper is the symmetrization of the SNO overpass time difference histograms which is performed to remove potential contributions of the overpass time difference to the bias; dependence of the SNO bias on time difference is demonstrated for SNPP CrIS and IASI-B at  $700\text{ cm}^{-1}$ . Lastly, the publicly available NASA CrIS L1B RU is used to define the CrIS measurement uncertainty. It is particularly valuable to have the CrIS uncertainty defined on every footprint and channel so that average uncertainties, specific to the subsets of data used in this study, can be accurately estimated. A globalized average measurement uncertainty would not have been able to capture the correct uncertainty magnitudes associated with the extreme cold temperatures of the high-latitude SNO datasets.

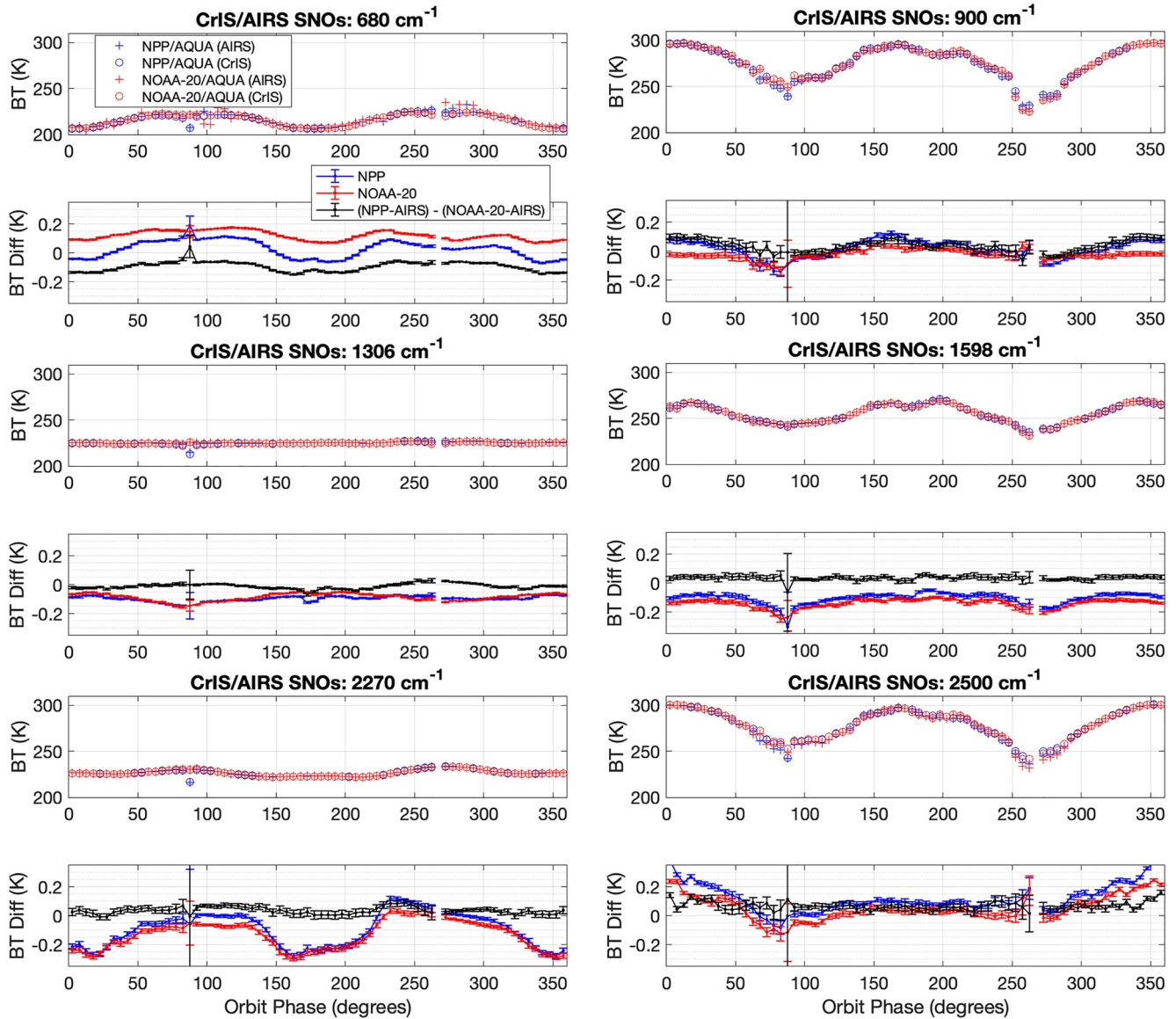


**Figure 12.** Cross-track Infrared Sounder (CrIS) orbital phase dependency of the CrIS/Atmospheric Infrared Sounder (AIRS) simultaneous nadir overpasses for (a) 680 cm<sup>-1</sup>, (b) 1,306 cm<sup>-1</sup>, (c) 2,270 cm<sup>-1</sup>, (d) 900 cm<sup>-1</sup>, (e) 1,598 cm<sup>-1</sup>, and (f) 2,500 cm<sup>-1</sup>. Mean brightness temperatures (BTs) (top panel) are shown with CrIS minus AIRS variance weighted BTs and NPP minus NOAA-20 variance weighted double difference BTs (bottom panels). Error bars on the differences indicate the 3σ uncertainty of the mean value within each 5° orbital phase bin.

SNO comparisons of the six hyperspectral sounders (3 IASI's, 2 CrIS's, 1 AIRS) reveal that the three IASI instruments appear to be in very good qualitative agreement and that the CrIS and IASI groups of instruments are in better agreement with each other than with the AIRS instrument. AIRS and IASI differences across the spectrum are generally less than 0.4 K, CrIS and IASI differences are generally less than 0.25 K, and CrIS and AIRS differences are generally less than 0.4 K. Comparison of the CrIS instruments via the three IASI's and AIRS shows that differences are generally less than 0.1 K across all three bands and that the two CrIS instruments statistically agree within their radiometric uncertainties except for the narrow 2,370 cm<sup>-1</sup> region where artifacts due to BT conversion are prone to occur. Differences between the CrIS instruments of 0.05 K at 700 cm<sup>-1</sup>, while less than the combined radiometric uncertainties of the CrIS instruments, are larger than the sampling uncertainty and thus indicate that the SNO methodology could inform on how to make the CrIS instruments more consistent with each other.

Strow et al. (2021) show differences between CrIS and AIRS, as well as the two CrIS instruments, using two techniques—SNOs and a statistical method (over a different time period and with different SNO analysis

techniques than those used here). Results from each the SNOs and statistical method agreed well to each other and are very quantitatively similar to those shown here. Wang and Chen (2019) likewise studied the differences between the two CrIS instruments, using both SNOs as well as other comparison techniques such as radiative transfer calculations and direct comparisons between the two CrISes, and again found very qualitatively similar results as to those shown here. This study thus offers affirmation of these previous analyses and provides radiometric measurement uncertainty estimates for each CrIS instrument which verify statistical agreement between the two CrIS instruments across the full spectrum for the time period analyzed (with the exception for where BT conversion issues occur around  $2,370\text{ cm}^{-1}$ ).

The orbital dependence of the CrIS double difference, using AIRS as the reference, is shown to be less than 100 mK for the selected channels. This indicates excellent consistency in the hardware, software, the orbital plane, and pre-launch and post-launch calibration methods of the SNPP and NOAA-20 CrIS sensors. In contrast, the CrIS-AIRS BT comparison shows orbital dependence with differences up to 300 mK for the channels shown. These orbital differences could be from a variety of systematic errors from either instrument or a combination of each and can be highly channel dependent. In this regard it is worth noting that the NASA CrIS L1B product includes an absolute RU for each CrIS footprint and channel which can be used in the interpretation of these results. No similar uncertainty estimate is currently available publicly for the NASA AIRS L1B or L1C products.

While the hyperspectral sounders compared here show impressive levels of agreement, improvements to their agreement would provide measurable benefits, particularly with regard to radiance climate trending. It is important to note that this work provides a snapshot in time of how the sounders compare and does not address stability issues. A large amount of work has been and is currently being done to merge the AIRS and CrIS datasets into a single data set with a common spectral resolution and continuity between data records from the different satellites (Strow et al., 2021) by accounting for biases between the instruments. However, regions where biases of unknown sources exist highlight the continued and urgent need for a more accurate on-orbit reference (Taylor et al., 2020; Tobin et al., 2016).

### Disclaimer

The scientific results and conclusions, as well as any views or opinions expressed herein, are those of the author(s) and do not necessarily reflect those of NOAA or the Department of Commerce.

### Data Availability Statement

The software used to find the SNOs analyzed in this study is called Collopak and is available from the University of Wisconsin—Madison Space Science and Engineering Center via the website at <https://www.ssec.wisc.edu/~gregq/collopak/index.html>. The specific tool used is the orbital navigation (OrbNav) Snotimes tool.

The NASA CrIS Level 1B FSR Version 3 radiances used for the intercomparisons in the study are available at the Goddard Earth Sciences Data and Information Services Center (GESDISC) via Earthdata (Revercomb and Strow 2020a, 2020b). SNPP CrIS radiances (SNPPCrISL1B) can be found here: <https://doi.org/10.5067/ZCRSHBM5HB23> and NOAA-20 CrIS (SNDRJ1CrISL1B) radiances can be found here: <https://doi.org/10.5067/LVEKYTNSRNKP>. A login account must be created to access the data. The CrIS radiometric uncertainties can be calculated using the formulas as described in the NASA CrIS Level 1B RU Description Document located online at [https://docserver.gesdisc.eosdis.nasa.gov/public/project/Sounder/NASA\\_CrIS\\_L1B\\_Radiometric\\_Uncertainty\\_v3.pdf](https://docserver.gesdisc.eosdis.nasa.gov/public/project/Sounder/NASA_CrIS_L1B_Radiometric_Uncertainty_v3.pdf).

The NASA AIRS Level 1C Version 6.7 radiances (AIRICRAD) used in this study are available at the Goddard Distributed Active Archive Center via Earthdata (Strow, 2019). A login account must be created. The AIRS spectral response functions used to condition the CrIS and IASI radiances are available from the UMBC Atmospheric Spectroscopy Lab via their website at <https://asl.umbc.edu/reports/srfs/> (Strow, 2020). The IASI Level 1C radiances used for the intercomparisons in the study are available from EUMETSAT via Earth Observation Portal at <http://archive.eumetsat.int/uscf/> (EUMETSAT, 2009). This product has a collection ID of EO:EUM:DAT:METOP:IASIL1C-ALL and more information can be found at <https://navigator.eumetsat.int/product/EO:EUM:DAT:METOP:IASIL1C-ALL>. A login account must be created to access data.

**Acknowledgments**

This research was funded by NOAA National Environmental Satellite, Data, and Information Service, Grant NA20NES4320003.

**References**

Aumann, H. H., Broberg, S., Elliott, D., Gaiser, S., & Gregorich, D. (2006). Three years of Atmospheric Infrared Sounder radiometric calibration validation using sea surface temperatures. *Journal of Geophysical Research*, 111(D16), D16S90. <https://doi.org/10.1029/2005JD006822>

Aumann, H. H., Broberg, S., Manning, E. M., Pagano, T., & Sutin, B. (2020). AIRS level 1C algorithm theoretical basis. Retrieved from <https://docsserver.gesdisc.eosdis.nasa.gov/public/project/AIRS/AIRICRAD.v6.7.ATBD.pdf>

Barbier, L., Pierangelo, C., & Faillot, M. (2021). Performance status of GSICS references IASI A/B/C. *GSICS Quarterly Newsletter Spring 2021 Issue*, 15(1), 9–11. <https://doi.org/10.25923/m6pq-w122>

Berndt, E., Smith, N., Burks, J., White, K., Esmaili, R., Kuciauskas, A., et al. (2020). Gridded satellite sounding retrievals in operational weather forecasting: Product description and emerging applications. *Remote Sensing*, 12(20), 3311. <https://doi.org/10.3390/rs12203311>

Bloch, C., Knuteson, R. O., Gambacorta, A., Nalli, N. R., Gartzke, J., & Zhou, L. (2019). Near-real-time surface-based CAPE from merged hyperspectral IR satellite sounder and surface meteorological station data. *Journal of Applied Meteorology and Climatology*, 58(8), 1613–1632. <https://doi.org/10.1175/jamc-d-18-0155.1>

Blumstein, D., Tournier, B., Cayla, F. R., Phulpin, T., Fjortoft, R., Buil, C., & Ponce, G. (2007). In-flight performance of the infrared atmospheric sounding interferometer (IASI) on METOP-A. In *Proceedings of SPIE 6684, atmospheric and environmental remote sensing data processing and utilization III: Readiness for GEOSS, 66840H*. <https://doi.org/10.1117/12.734162>

Brindley, H., Bantges, R., Russell, J., Murray, J., Dancel, C., Belotti, C., & Harries, J. (2015). Spectral signatures of Earth's climate variability over 5 Years from IASI. *Journal of Climate*, 28(4), 1649–1660. <https://doi.org/10.1175/jcli-d-14-00431.1>

Cao, C., Ciren, P., Goldberg, M., & Weng, F. (2005). Intersatellite calibration of HIRS from 1980 to 2003 using the simultaneous nadir overpass (SNO) method for improved consistency and quality of climate data. In *Paper presented at International TOVS study conference, Beijing, China*.

Cao, C., Goldberg, M., Weng, F., & Zou, C.-Z. (2005). Simultaneous Nadir Overpasses for NOAA-6 to NOAA-17 satellites from 1980 to 2003 for the intersatellite calibration of radiometers. In *NOAA technical report NESDIS 118*. US Department of Commerce.

Cao, C., Weinreb, M., & Xu, H. (2004). Predicting simultaneous nadir overpasses among polar-orbiting meteorological satellites for the intersatellite calibration of radiometers. *Journal of Atmospheric and Oceanic Technology*, 21(4), 537–542. [https://doi.org/10.1175/1520-0426\(2004\)021<0537:PSNOAP>2.0.CO;2](https://doi.org/10.1175/1520-0426(2004)021<0537:PSNOAP>2.0.CO;2)

Chen, Y., Han, Y., & Weng, F. (2016). Characterization of long-term stability of suomi NPP cross-track infrared sounder spectral calibration. *IEEE Transactions on Geoscience and Remote Sensing*, 55(2), 1147–1159. <https://doi.org/10.1109/TGRS.2016.2620438>

Della Fera, S., Fabiano, F., Raspollini, P., Ridolfi, M., Cortesi, U., Barbara, F., & von Hardenberg, J. (2022). On the use of IASI spectrally resolved radiances to test the EC-Earth climate model (v3.3.3) in clear-sky conditions. *EGU sphere*. <https://doi.org/10.5194/egusphere-2022-479>

EUMETSAT. (2009). IASI level 1C—All spectral samples—Metop—Global. [Dataset]. European Organisation for the Exploitation of Meteorological Satellites. Retrieved from <https://navigator.eumetsat.int/product/EO-EUM:DAT:METOP:IASI:1C-ALL>

Goldberg, M., Ohring, G., Butler, J., Cao, C., Datla, R., Doelling, D., et al. (2011). The global space-based inter-calibration system. *Bulletin of the American Meteorological Society*, 92(4), 467–475. <https://doi.org/10.1175/2010BAMS2967.1>

Gyanesh, C., Hewison, T., Fox, N., Wu, X., Xiong, X., & Blackwell, W. (2013). Overview of intercalibration of satellite instruments. *IEEE Transactions on Geoscience and Remote Sensing*, 51(3), 1056–1080. <https://doi.org/10.1109/TGRS.2012.2228654>

Hilton, F., Armante, R., August, T., Barnett, C., Bouchard, A., Camy-Peyret, C., et al. (2012). Hyperspectral Earth observation from IASI: Five years of accomplishments. *Bulletin of the American Meteorological Society*, 93(3), 347–370. <https://doi.org/10.1175/bams-d-11-00027.1>

Iacovazzi, R., Jr., & Cao, C. (2008). An AIRS-IASI inter-comparison. *GSICS Quarterly Newsletter*, 2(2), 2–3. Retrieved from [https://www.star.nesdis.noaa.gov/smcd/GCC/documents/newsletter/GSICS\\_Quarterly\\_Vol2No2\\_2008.pdf](https://www.star.nesdis.noaa.gov/smcd/GCC/documents/newsletter/GSICS_Quarterly_Vol2No2_2008.pdf)

Kilymis, D., Barbier, L., Kangah, Y., Jacqueline, E., Lenot, X., Ansart, J., et al. (2023). IASI radiometric error uncertainty budget and inter-comparison results. In *Proceedings of the 24th international TOVS study conference (ITSC-24), Tromso, Norway, 15–22 March 2023*.

Maier, J., & Knuteson, R. (2022). Data fusion of GEO FY-4A GIIRS and LEO hyperspectral infrared sounders with surface observations: A Hong Kong case study. *Journal of Atmospheric and Oceanic Technology*, 39(2), 259–270. <https://doi.org/10.1175/jtech-d-21-0080.1>

Motteler, H. E., & Strow, L. L. (2019). AIRS deconvolution and the translation of AIRS-to-CrIS radiances with applications for the IR climate record. *IEEE Transactions on Geoscience and Remote Sensing*, 57(3), 1793–1803. <https://doi.org/10.1109/TGRS.2018.2869170>

Nagle, F. W., & Holz, R. (2009). Computationally efficient methods of collocating satellite, aircraft, and ground observations. *Journal of Atmospheric and Oceanic Technology*, 26(8), 1585–1595. <https://doi.org/10.1175/2008JTECHA1189.1>

Pagano, T. S., Aumann, H., Hagan, D., & Overoye, K. (2003). Prelaunch and in-flight radiometric calibration of the atmospheric infrared sounder (AIRS). *IEEE Transactions on Geoscience and Remote Sensing*, 41(2), 265–273. <https://doi.org/10.1109/TGRS.2002.808324>

Pagano, T. S., Aumann, H. H., Broberg, S. E., Cañas, C., Manning, E. M., Overoye, K. O., & Wilson, R. C. (2020). SI-traceability and measurement uncertainty of the atmospheric infrared sounder version 5 level 1B radiances. *Remote Sensing*, 12(8), 1338. <https://doi.org/10.3390/rs12081338>

Payne, V. H., Kulawik, S. S., Fischer, E. V., Brewer, J. F., Huey, L. G., Miyazaki, K., et al. (2022). Satellite measurements of peroxyacetyl nitrate from the cross-track infrared sounder: Comparison with ATom aircraft measurements. *Atmospheric Measurement Techniques*, 15(11), 3497–3511. <https://doi.org/10.5194/amt-15-3497-2022>

Revercomb, R., & Strow, L. (2020a). JPSS-1 CrIS level 1B full spectral resolution V3 [Dataset]. Goddard Earth Sciences Data and Information Services Center (GES DISC). <https://doi.org/10.5067/LVEKYTNSRNP>

Revercomb, R., & Strow, L. (2020b). Suomi NPP CrIS level 1B full spectral resolution V3 [Dataset]. Goddard Earth Sciences Data and Information Services Center (GES DISC). <https://doi.org/10.5067/ZCRSHBMS5HB23>

Smith, N., & Barnett, C. D. (2020). CLIMCAPS observing capability for temperature, moisture, and trace gases from AIRS/AMSU and CrIS/ATMS. *Atmospheric Measurement Techniques*, 13(8), 4437–4459. <https://doi.org/10.5194/amt-13-4437-2020>

Smith, W. L., Zhang, Q., Shao, M., & Weisz, E. (2020). Improved severe weather forecasts using LEO and GEO satellite soundings. *Journal of Atmospheric and Oceanic Technology*, 37(7), 1203–1218. <https://doi.org/10.1175/jtech-d-19-0158.1>

Strow, L. L. (2019). AIRS/Aqua L1C Infrared (IR) resampled and corrected radiances V6.7 [Dataset]. Goddard Earth Sciences Data and Information Services Center (GES DISC). <https://doi.org/10.5067/VWD3DR007UEN>

Strow, L. L. (2020). AIRS spectral response functions, UMBC atmospheric spectroscopy Lab. Retrieved from <https://asl.umbc.edu/reports/srfs/>

Strow, L. L., Hannon, S. E., Weiler, M., Overoye, K., Gaiser, S. L., & Aumann, H. H. (2003). Prelaunch spectral calibration of the atmospheric infrared sounder (AIRS). *IEEE Transactions on Geoscience and Remote Sensing*, 41(2), 274–286. <https://doi.org/10.1109/TGRS.2002.808245>

Strow, L. L., Hepplewhite, C., Motteler, H., Buczkowski, S., & DeSouza-Machado, S. A. (2021). Climate hyperspectral infrared radiance product (CHIRP) combining the AIRS and CrIS satellite sounding record. *Remote Sensing*, 13(3), 418. <https://doi.org/10.3390/rs13030418>

- Strow, L. L., Motteler, H., Tobin, D., Revercomb, H., Hannon, S., Buijs, H., et al. (2013). Spectral calibration and validation of the cross-track infrared sounder on the suomi NPP satellite. *Journal of Geophysical Research: Atmospheres*, *118*(22), 12486–12496. <https://doi.org/10.1002/2013JD020480>
- Taylor, J. K., Revercomb, H. E., Best, F. A., Tobin, D. C., & Gero, P. J. (2020). The infrared absolute radiance interferometer (ARI) for CLARREO. *Remote Sensing*, *12*(12), 1915. <https://doi.org/10.3390/rs12121915>
- Tobin, D. C., Holz, R., Nagle, F., & Revercomb, H. (2016). Characterization of the Climate Absolute Radiance and Refractivity Observatory (CLARREO) ability to serve as an infrared satellite intercalibration reference. *Journal of Geophysical Research: Atmospheres*, *121*(8), 4258–4271. <https://doi.org/10.1002/2016JD024770>
- Tobin, D. C., Dutcher, S., & Revercomb, H. (2010). Evaluation of IASI and airs spectral radiances using simultaneous nadir overpasses. In *Paper presented at 2nd international IASI conference, cent. Natl. Etud. Spatiales, Sévrier, France*. Retrieved from [http://smc.cnes.fr/IASI/presents\\_conf2.htm](http://smc.cnes.fr/IASI/presents_conf2.htm)
- Tobin, D. C., Revercomb, H., Knuteson, R., Best, F., Smith, W., Ciganovich, N., et al. (2006). Radiometric and spectral validation of atmospheric infrared sounder observations with the aircraft-based scanning high-resolution interferometer sounder. *Journal of Geophysical Research*, *111*(D9), D09S02. <https://doi.org/10.1029/2005JD006094>
- Tobin, D. C., Revercomb, H., Knuteson, R., Taylor, J., Best, F., Borg, L., et al. (2013a). Suomi-NPP CrIS radiometric calibration uncertainty. *Journal of Geophysical Research: Atmospheres*, *118*(18), 10589–10600. <https://doi.org/10.1002/jgrd.50809>
- Tobin, D. C., Revercomb, H., Taylor, J., Knuteson, R., DeSlover, D., & Borg, L. (2013b). Calibration/validation results for the cross-track infrared sounder (CrIS) on suomi-NPP. In *Imaging and applied optics, OSA technical digest (online) (optica Publishing group), paper FT11C.2*. UW-Madison Space Science and Engineering Center, University of Maryland Baltimore County Atmospheric Spectroscopy Laboratory. (2022). NASA cross-track infrared sounder (CrIS) level 1B radiometric uncertainty description document. Version 3. Retrieved from [https://docserver.gesdisc.eosdis.nasa.gov/public/project/Sounder/NASA\\_CrIS\\_L1B\\_Radiometric\\_Uncertainty\\_v3.pdf](https://docserver.gesdisc.eosdis.nasa.gov/public/project/Sounder/NASA_CrIS_L1B_Radiometric_Uncertainty_v3.pdf)
- Wang, L., Cao, C., & Ciren, P. (2007). Assessing NOAA-16 HIRS radiance accuracy using simultaneous nadir overpass observations from AIRS. *Journal of Atmospheric and Oceanic Technology*, *24*(9), 1546–1561. <https://doi.org/10.1175/JTECH2073.1>
- Wang, L., & Chen, Y. (2019). Inter-comparing SNPP and NOAA-20 CrIS toward measurement consistency and climate data records. *IEEE Journal of Selected Topics in Applied Earth Observations and Remote Sensing*, *12*(7), 2024–2031. <https://doi.org/10.1109/JSTARS.2019.2891701>
- Wang, L., Goldberg, M., Wu, X., Cao, C., Iacovazzi, R. A., Yu, F., & Li, Y. (2011). Consistency assessment of atmospheric infrared sounder and infrared atmospheric sounding interferometer radiances: Double differences versus simultaneous nadir overpasses. *Journal of Geophysical Research*, *116*(D11), D11111. <https://doi.org/10.1029/2010JD014988>
- Wang, L., Han, Y., Jin, X., Chen, Y., & Tremblay, D. A. (2015). Radiometric consistency assessment of hyperspectral infrared sounders. *Atmospheric Measurement Techniques*, *8*(11), 4831–4844. <https://doi.org/10.5194/amt-8-4831-2015>
- Wang, L., Tremblay, D. A., Han, Y., Esplin, M., Hagan, D. E., Predina, J., et al. (2013). Geolocation assessment for CrIS sensor data records. *Journal of Geophysical Research: Atmospheres*, *118*(22), 12690–12704. <https://doi.org/10.1002/2013JD020376>
- Wang, L., Zhang, B., Tremblay, D., & Han, Y. (2017). Improved scheme for Cross-track Infrared Sounder geolocation assessment and optimization. *Journal of Geophysical Research: Atmospheres*, *122*(1), 519–536. <https://doi.org/10.1002/2016JD025812>
- Worden, H. M., Francis, G. L., Kulawik, S. S., Bowman, K. W., Cady-Pereira, K., Fu, D., et al. (2022). TROPES/CrIS carbon monoxide profile validation with NOAA GML and ATom in situ aircraft observations. *Atmospheric Measurement Techniques*, *15*(18), 5383–5398. <https://doi.org/10.5194/amt-15-5383-2022>